

# Swirling flow of viscoelastic fluids. Part 1. Interaction between inertia and elasticity

By JASON R. STOKES<sup>1</sup>, LACHLAN J. W. GRAHAM<sup>2</sup>,  
NICK J. LAWSON<sup>1</sup> AND DAVID V. BOGER<sup>1</sup>

<sup>1</sup>Department of Chemical Engineering, The University of Melbourne, Parkville 3052, Australia

<sup>2</sup>Advanced Fluid Dynamics Laboratory, CSIRO Building Construction and Engineering,  
Graham Road, Highett 3190, Australia

(Received 29 December 1998 and in revised form 11 October 1999)

A torsionally driven cavity, consisting of a fully enclosed cylinder with rotating bottom lid, is used to examine the confined swirling flow of low-viscosity Boger fluids for situations where inertia dominates the flow field. Flow visualization and the optical technique of particle image velocimetry (PIV) are used to examine the effect of small amounts of fluid elasticity on the phenomenon of vortex breakdown. Low-viscosity Boger fluids are used which consist of dilute concentrations of high molecular weight polyacrylamide or semi-dilute concentrations of xanthan gum in a Newtonian solvent. The introduction of elasticity results in a 20% and 40% increase in the minimum critical aspect ratio required for vortex breakdown to occur using polyacrylamide and xanthan gum, respectively, at concentrations of 45 p.p.m. When the concentrations of either polyacrylamide or xanthan gum are raised to 75 p.p.m., vortex breakdown is entirely suppressed for the cylinder aspect ratios examined. Radial and axial velocity measurements along the axial centreline show that the alteration in existence domain is linked to a decrease in the magnitude of the peak in axial velocity along the central axis. The minimum peak axial velocities along the central axis for the 75 p.p.m. polyacrylamide and 75 p.p.m. xanthan gum Boger fluids are 67% and 86% lower in magnitude, respectively, than for the Newtonian fluid at Reynolds number of  $Re \approx 1500$ – $1600$ . This decrease in axial velocity is associated with the interaction of elasticity in the governing boundary on the rotating base lid and/or the interaction of extensional viscosity in areas with high velocity gradients. The low-viscosity Boger fluids used in this study are rheologically characterized and the steady complex flow field has well-defined boundary conditions. Therefore, the results will allow validation of non-Newtonian constitutive models in a numerical model of a torsionally driven cavity flow.

---

## 1. Introduction

A torsionally driven cavity produces a swirling flow field under well-defined boundary conditions and provides a suitable simple geometry for numerical study of the flow of viscoelastic fluids. In addition, swirling flow is common throughout process engineering and therefore an understanding of the fundamental behaviour of non-Newtonian fluids owing to swirl has industrial relevance.

A torsionally driven cavity is displayed in figure 1 and consists of a fully enclosed cylinder in which rotation of the bottom lid produces a primary flow in the azimuthal direction and a secondary flow in the radial and axial directions. Centrifugal or

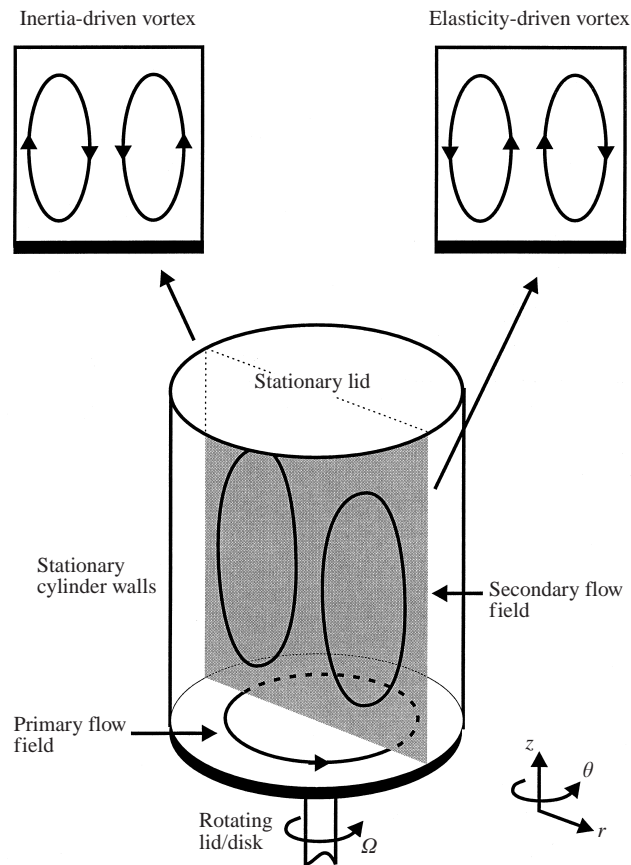


FIGURE 1. Torsionally driven cavity flow fields.

inertial forces cause the fluid to experience a force directed radially outwards along the disk, producing a secondary flow pattern, as shown in the top left-hand corner of figure 1. This secondary flow vortex is observed for Newtonian fluids and will be termed ‘Newtonian-like’ flow or an ‘inertia driven vortex’. In the case of elastic fluids, normal stresses cause the fluid to experience a force directed radially inwards along the disk, opposing centrifugal effects, producing a secondary flow pattern as shown in the top right-hand corner of figure 1. This secondary flow vortex is termed ‘reverse flow’ or an ‘elastic driven vortex’. The competition between inertial and elastic effects can produce a wide variety of complicated secondary flow fields.

The behaviour of dilute flexible and semi-rigid polymer solutions, with a constant viscosity, in the torsionally driven cavity is investigated. Constant-viscosity elastic liquids, commonly referred to as Boger fluids (Boger 1977/78), are used to ensure that changes in the flow kinematics are associated purely with fluid elasticity and cannot be confused with effects due to shear-thinning viscosity which are found in all previous experimental work using non-Newtonian fluids in a confined swirling flow (Hill 1972; Böhme, Rubart & Stenger 1992; Day *et al.* 1996; Escudier & Cullen 1996).

This paper investigates the influence of elasticity in an inertia dominated flow in the parameter space where vortex breakdown is observed for Newtonian fluids. Part 2 (Stokes *et al.* 2001) investigates the transition from an inertia dominated flow to

an elasticity dominated flow by using several flexible polymer Boger fluids of varying elasticity levels and a semi-rigid polymer Boger fluid. The aim of the research is to report on the influence of elasticity in a complex flow field with and without the presence of inertia. The well-defined boundary conditions of the torsionally driven cavity make it an ideal geometry for the testing of non-Newtonian constitutive equations for numerical solution as a precursor to solving more difficult and complex swirling flow problems such as those associated with mixing.

## **2. Previous work**

The following section will review previous investigations on the flow behaviour of both Newtonian and non-Newtonian fluids in the torsionally driven cavity.

### *2.1. Vortex breakdown and the confined swirling flow of Newtonian fluids*

Vortex breakdown refers to the situation where a sudden transition of a vortex flow structure occurs with an abrupt change in character. The breakdown is usually associated with the development of a flow stagnation point and often with regions of reversed axial flow. Vortex breakdown was reportedly first observed experimentally as the ‘bursting’ of trailing-edge vortices from aircraft travelling at high angles of attack by Peckham & Atkinson (1957), Elle (1960), Werlé (1960) and Lambourne & Bryer (1961). Detailed investigations of breakdown on delta wings have been limited by the complicated nature of the leading-edge vortex, its unsteadiness and a lack of axial symmetry. Harvey (1962) observed vortex breakdown in a vortex tube where air travels axially along a circular tube with the degree of swirl imparted on the air controlled by a set of adjustable vanes. The introduction of a diverging tube by Sarpakaya (1971) allowed the characterization of several types of breakdown forms and, in particular, he observed the transformation between the two main types of breakdown – asymmetric ‘spiral-type’ and axisymmetric ‘bubble-type’ – by increasing the degree of swirl. The development of more refined experiments allowed the primary conditions necessary for vortex breakdown to be established as a high degree of swirl, a positive or adverse pressure gradient and a divergence of the stream tubes in the vortex core immediately upstream of the breakdown (Hall 1972). This was investigated further by using an enclosed cylinder with rotating endwall (Escudier 1984). In this case, the axisymmetric geometry and well-defined boundary conditions produced a well-posed problem, ideal for the numerical solution of the Navier–Stokes equations (Lopez 1990).

Vortex breakdown has been widely studied over the last 40 years with the first theories proposed by Jones (1960), Squire (1960), Ludweig (1961), and Benjamin (1962). Detailed discussion on the mechanisms and theories governing breakdown may be found in review articles by Hall (1972), Leibovich (1978, 1984), Escudier (1988), and Delerey (1994). More recent discussions on the phenomena have been made by Berger & Erlebacher (1995), Keller (1995), Rusak (1996), and Wang & Rusak (1997). However, there is still no general consensus as to the underlying mechanism leading to breakdown.

In the confined cylindrical swirling flow of Newtonian liquids, in which the fluid is situated in an enclosed cylinder with rotating bottom lid (also referred to as a disk or endwall), the rotation of the lid produces a non-uniform centrifugal force along the base and a secondary flow in the cylinder normal to the primary flow is generated. Here, an Ekman layer is present on the rotating lid with a thickness of the order

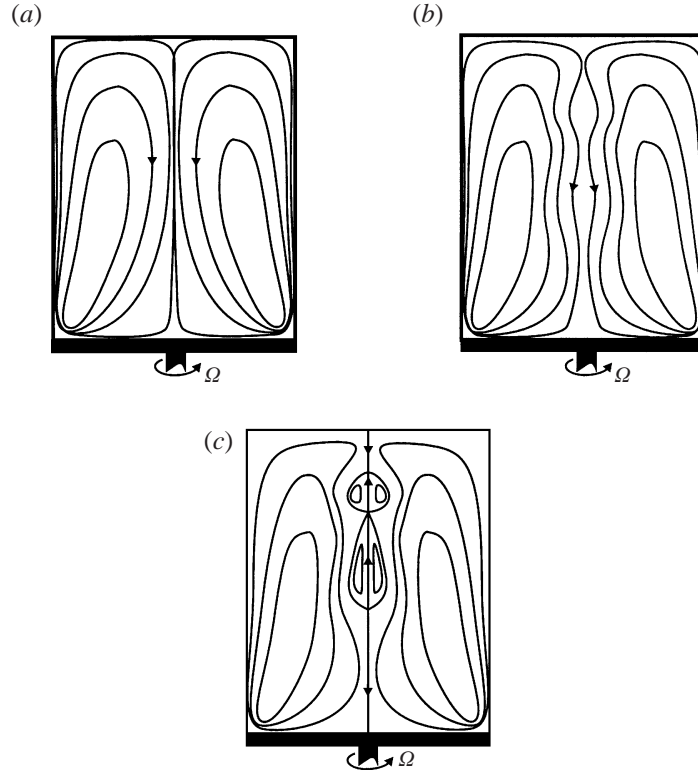


FIGURE 2. Secondary flow patterns for a Newtonian fluid at conditions showing (a) inertia driven vortex, (b) pre-incipient breakdown, and (c) vortex breakdown.

$(1/Re)^{0.5}$  (Lopez 1990) where  $Re$  is the Reynolds number defined by:

$$Re = \frac{\rho(2\pi\Omega)R^2}{\eta}, \quad (1)$$

where  $\rho$  is the density ( $\text{kg m}^{-3}$ ),  $\Omega$  is the disk rotation rate ( $\text{s}^{-1}$ ),  $R$  is the disk radius (m), and  $\eta$  is the viscosity (Pa s). The Ekman layer acts as a centrifugal pump by driving the fluid outwards along the rotating base, up the sidewalls, inwards along the stationary lid and down the central axis in a spiral motion where it is then sucked back into the boundary layer, as depicted in figure 2(a). As the rotation rate of the disk is increased, a widening of the vortex core near the disk is observed with a waviness in the sectional streamline patterns as illustrated in figure 2(b). Further increases in disk speed results in the production of a stagnation point on the central axis and a weak recirculation zone which is characteristic of an axisymmetric vortex breakdown bubble and shown in figure 2(c).

Vortex breakdown in an enclosed cylinder with a rotating lid was first observed experimentally using flow-visualization techniques by Vogel (1968, 1975), Hill (1972), and Ronnenberg (1977) for a limited range of parameter space and with only one breakdown bubble observed. Escudier (1984) observed the formation of up to three breakdown bubbles and produced a detailed diagram, represented in figure 3, showing the existence domain of vortex breakdown with respect to two governing dimensionless groups, the cylinder aspect ratio ( $H/R$ ) and the Reynolds number defined in (1) where  $H$  is defined as the cylinder height. Escudier (1984) also observed that the breakdown

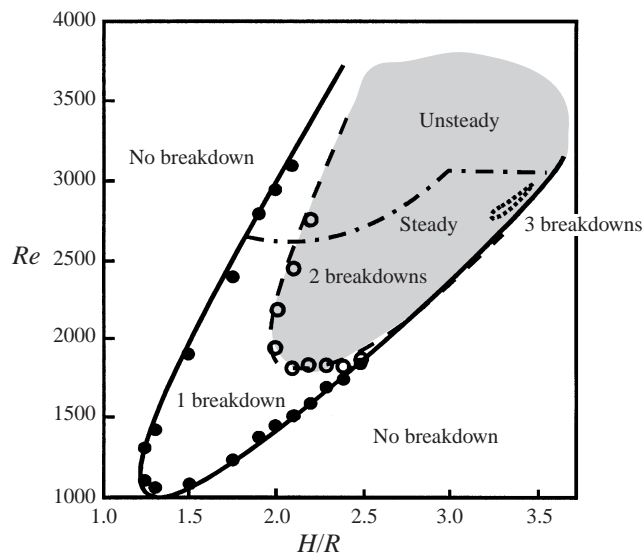


FIGURE 3. Existence domain of vortex breakdown for Newtonian fluids (Escudier 1984). Circular symbols represent experimental points produced for a Newtonian fluid in the current paper.

regions were highly axisymmetric, which supported his view that vortex breakdown is inherently axisymmetric and departures from axisymmetry are the result of instabilities not directly associated with the breakdown process. The recirculation zone inside the breakdown region was observed to contain low interior velocities. An oscillatory flow regime, where the breakdown bubbles move up and down in a periodic manner, was also observed at high Reynolds numbers (above  $Re \approx 2600$  for  $H/R > 1.8$ ) with vortex breakdown still highly axisymmetric. The flow was ultimately observed to become unsteady and then turbulent with a further increase in the Reynolds number. Fujimura, Koyama & Hyan (1997) examined the location of the stagnation points during spin-up and spin-down of the rotating lid. He found that equilibrium after spin-up from rest was reached after more than 25 s with conditions  $1970 < Re < 2450$  and  $H/R = 2.5$ .

There are only a few reports of measurements of velocity distributions in the disk and cylinder system for Newtonian fluids. In the absence of breakdown, tangential velocity measurements have been made by Bien & Penner (1970) and radial and tangential velocity measurements were made by Hill (1972). Prasad & Adrian (1993) have also demonstrated the use of the optical technique stereoscopic particle image velocimetry (PIV) to obtain measurements of the tangential, radial and axial velocity profiles for a Newtonian fluid at low Reynolds number. However, only a limited set of velocity measurements have been made in the presence of breakdown by Ronnenberg (1977) and Buchave *et al.* (1991).

The cylinder with rotating lid provides the simplest geometry in which vortex breakdown is observed. This flow field is therefore ideal for numerical studies into the vortex breakdown phenomena using the time-dependent Navier–Stokes equations. Investigation into vortex breakdown at steady-state conditions using the numerical solution of the axisymmetric Navier–Stokes equations has been primarily performed by Lugt & Abboud (1987), Lopez (1990), Brown & Lopez (1990), Tsitverbilt (1993), and Gelfgat, Bar-Yoseph & Solan (1996). In the work by Lopez (1990), the numerical model was validated by comparing the predicted streamlines with the streaklines ob-

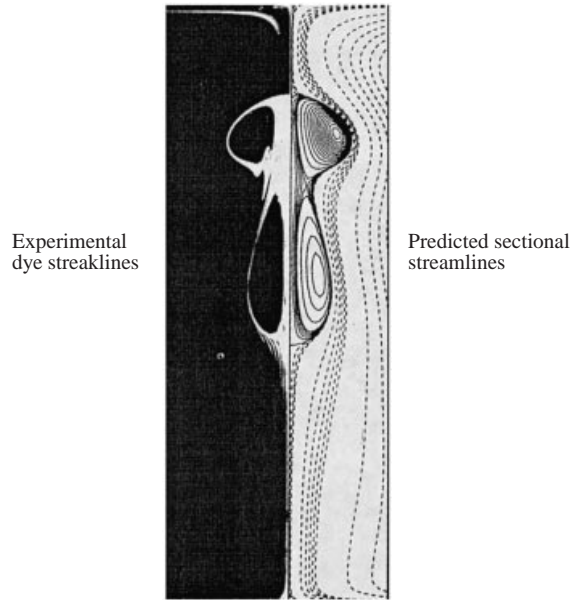


FIGURE 4. Comparison between experimentally observed dye-lines (Escudier 1984) and numerically predicted sectional streamline patterns (Lopez 1990) of vortex breakdown for a Newtonian fluid at  $Re = 2494$  and  $H/R = 2.5$ .

served from the flow-visualization images of Escudier (1984) with excellent agreement, as shown in figure 4. Brydon & Thompson (1998) were able to accurately predict the entire existence domain diagram of Escudier (1984).

Lopez (1990) describes the breakdown process as the result of the advection of angular momentum towards the central axis as the fluid flows radially inwards along the stationary lid from the corner of the sidewall at Reynolds numbers a little below those required for breakdown ( $Re \approx 1600$ – $1800$  for  $H/R = 2.5$ ). Preservation of the angular momentum causes the angular velocity to increase, and consequently an increase in centrifugal acceleration to a local maxima results as the fluid flows axially down in the centre of the cylinder towards the rotating lid. The stream surfaces then deform and take on a concave shape resulting in a stationary centrifugal (or inertial) wave, as shown in the streamlines of figure 2(b). The amplitude of the inertial waves increases and their wavelength decreases with further increases towards the Reynolds number required for breakdown. The associated axial deceleration is then large enough to cause the flow to stagnate under the crest of the wave and cause an adverse pressure gradient resulting in vortex breakdown (figure 2c).

A ratio of swirl to axial velocity has been well established as a useful criteria for the breakdown of a vortex (e.g. Hall 1972; Delerey 1994). It indicates that when the swirl ( $V_\phi$ ) is large relative to the axial velocity ( $V_z$ ), a stagnation point can form, and breakdown results. The common form of the criteria is as a swirl angle ( $\phi_v$ ) which is stated by Hall (1972) as:

$$\phi_v = \tan^{-1} \left( \frac{V_\phi}{V_z} \right). \quad (2)$$

Hall (1972) states that the maximum value of  $\phi_v$  upstream of breakdown is invariably greater than  $40^\circ$ . In the torsionally driven cavity, the numerical analysis of Lugt & Abboud (1987) showed that Hall's (1972) criteria were met with a value of the swirl

angle just below the stationary lid increasing to  $40^\circ$  once breakdown took place for  $H/R = 2$ .

Lopez (1990) and Brown & Lopez (1990) postulated that the recirculation zones result from the ‘generation of negative azimuthal vorticity through the stretching and tilting of vortex lines’ and that this is a necessary condition for the occurrence of vortex breakdown. They also applied their theory to the swirling pipe flow and established an alternative criteria for the occurrence of breakdown based on the relationship between the angle of the velocity vector or swirl angle and the angle of the vorticity vector ( $\phi_\omega$ ) on stream surfaces upstream of breakdown such that:

$$\phi_v > \phi_\omega, \quad (3)$$

where  $\phi_\omega = \tan^{-1}(\omega_\phi/\omega_z)$  while  $\omega_\phi$  and  $\omega_z$  are the azimuthal and radial components of vorticity, respectively.

Gelfgat *et al.* (1996), similarly to Lopez (1990), conclude that a necessary condition for vortex breakdown is a concave form of the stream surfaces, which may be considered as the cause in the change in sign of the azimuthal component of vorticity. However, Gelfgat *et al.* (1996) also show that vortex breakdown does not necessarily occur when the azimuthal vorticity is negative, or when the stream surfaces are concave in shape, by observing these conditions at low cylinder aspect ratios where vortex breakdown does not occur at any Reynolds number.

The oscillatory instability and unsteady flow behaviour which Escudier (1984) observed at high Reynolds number, as shown in figure 3, has been investigated by Sørensen & Daube (1989), Lopez (1990), Lopez & Perry (1992), Liao & Young (1995), Sørensen & Christensen (1995), and Gelfgat *et al.* (1996). The study of time-dependent flows in the torsionally driven cavity flow gives an insight into the changing kinematics of the various flow structures observed at high Reynolds number.

Related works involving the cylinder geometry include the corotation or counter-rotation of two lids and the use of an open cylinder where a single lid is rotated with a free surface. Roesner (1990) investigated experimentally vortex breakdown in a cylinder with two rotating lids and found that when at incipient breakdown, corotation of the lids resulted in breakdown while counter-rotation resulted in the disappearance of the breakdown bubble. Numerical investigations into the two rotating lid systems have been conducted by Valentine & Jahnke (1994), Lopez (1995), Gelfgat *et al.* (1996) and Watson & Neitzel (1996). Watson & Neitzel (1996) found that the criteria of Brown & Lopez (1990) were met at the location of the breakdown bubble in their flow domain. However, the criteria were not met upstream of breakdown, nor at the incipient state of breakdown, which questions the use of the criteria of Brown & Lopez (1990) as a predictive tool. Spohn, Mory & Hopfinger (1993, 1998) examined experimentally the secondary flow in an open cylinder with one rotating lid and found that the conditions for vortex breakdown changed noticeably from those observed for a closed cylinder. The differences to the closed cylinder case include: breakdown was at a lower Reynolds number; a breakdown bubble was present even at the maximum Reynolds number tested ( $Re \approx 3500$ ); breakdown was observed at aspect ratio as low as  $H/R = 0.5$ ; and breakdown bubbles were generally much larger in size. A breakdown bubble attached to the free surface was also observed which cannot be explained by classical vortex breakdown theories (e.g. Benjamin 1962; Ludweig 1961) which assumed a cylindrical vortex core upstream of breakdown.

In summary, in the confined swirling flow of Newtonian fluids, inertia causes fluid to be forced outwards along the rotating lid and creates a secondary flow normal to the primary flow. In the subcritical state prior to breakdown, the divergence of

Observation	$Re_0$	$We$	$El$
<i>Hill (1972) <math>H/R = 1</math> 0.016–0.52% polyacrylamide in 10–54% glycerol–water</i>			
‘reverse’ flow (6a)	< 1	< 0.5	0.1–60
Unsteady flow/instability	0.1–0.4	0.3–0.5	0.7–4
Counter-rotating vortices (6b)	0.2–20	0.3–0.5	0.02–2
‘Newtonian’ flow (2a)	0.4–90	0.2–0.4	0.004–0.04
<i>Day et al. (1996) <math>H/R = 1.8</math> 2.5% polyacrylamide in water</i>			
‘Reverse’ flow (6a)	0.88	0.88	1
Instability	1.57	0.94	< 0.6
<i>Escudier &amp; Cullen (1996) <math>1.5 &lt; H/R &lt; 2.84</math> 0.75–1.5% carboxymethylcellulose in water or glucose–water</i>			
Counter-rotating vortices (6b)	7–174	< 0.014	< 0.002
<i>Böhme et al. (1992) <math>1 &lt; H/R &lt; 3</math> 0.1% carboxymethylcellulose in 60–80% glycerol–water</i>			
Vortex breakdown (2c)	> 1000	—	—

TABLE 1. Summary of previous experimental observations made using non-Newtonian fluids. Figure numbers corresponding to the observations are given in parentheses.

axial streamlines leads to an adverse pressure gradient down the central axis and the sectional streamline patterns form stationary inertial waves. Once a critical swirl level for a supercritical state is reached, stagnation occurs along the central axis and the inertial waves propagate upstream, resulting in vortex breakdown.

## 2.2. Confined swirling flow of non-Newtonian fluids

The confined swirling flow of non-Newtonian fluids was realized as an experimental test case for the validation of fluid constitutive equations by Hill, Huppler & Bird (1966). It was demonstrated that for a highly elastic and shear-thinning fluid, the rotation of the disk generated a secondary flow field which was in the opposite direction to that for a Newtonian fluid as a result of induced normal stresses in the fluid. Hill (1969, 1972), Böhme *et al.* (1992), Day *et al.* (1996), Escudier & Cullen (1996) and Wusch & Böhme (1996) have all used fluids which are highly shear-thinning and contain varying amount of elasticity. A summary for previous experimental observations of non-Newtonian fluids in the torsionally driven cavity is presented in table 1.

The introduction of non-Newtonian fluids into the confined swirling flow experiment creates two additional independent sets of parameters into the problem: elasticity and shear-thinning. Shear-thinning may be represented by either a single or group of shear-thinning parameters which may be found in numerous viscosity models (eg. Carreau models and ‘power law’ models, see Bird, Armstrong & Hassager 1987a). If the fluid is shear-thinning, then the Reynolds number is based on the zero-shear rate viscosity ( $\eta_0$ ) and given the symbol  $Re_0$ . Elasticity is typically represented by a Weissenberg number ( $We$ ) which is measured by evaluating the ratio of the characteristic time of the fluid (eg. Maxwell relaxation time:  $\lambda_M$  and characteristic time of

the process (eg.  $1/2\pi\Omega$ ). The Weissenberg number may be evaluated as follows:

$$We = \lambda_M 2\pi\Omega. \quad (4)$$

Another dimensionless number used is the elasticity number ( $El$ ) which measures the ratio of the elastic forces to the inertial forces and may be represented as follows:

$$El = \frac{We}{Re} = \frac{\lambda_M \eta_0}{\rho R^2}. \quad (5)$$

A feature of the elasticity number is that it is independent of the rotation rate of the lid, provided the relaxation time and viscosity are constant and not shear rate dependent.

Böhme *et al.* (1992) performed experiments using low concentrations (0.1%) of carboxymethylcellulose in glycerol–water solvents to produce two highly shear-thinning solutions in order to investigate the effect of shear-thinning on vortex breakdown. A shear-thinning parameter ( $\beta$ ) which was independent of the rotation rate of the disk was defined by:

$$\beta = \frac{\eta_\delta(\eta_0 - \eta_z)}{\rho \tau_* c d^2}, \quad (6)$$

where  $\eta_\delta$  is the solvent viscosity,  $c$  is the polymer concentration,  $d$  is the diameter of the disk, and  $\tau_*$  is a constant reference stress which was determined by fitting the viscosity to a master curve. The fluids investigated had shear-thinning parameters of  $\beta = 0.13$  and  $\beta = 1.0$ , with  $\beta = 0$  indicating a Newtonian fluid. Experiments were performed at high Reynolds numbers where inertial dominated and the elasticity was considered negligible, although no measurements of any elastic material properties were presented. ‘Newtonian-like’ flow and axisymmetric vortex breakdown were observed by Böhme *et al.* (1992) for the shear-thinning fluids. However, the existence domain for vortex breakdown decreased in size and was shifted to higher values of the cylinder aspect ratio as the degree of shear-thinning was increased. The resulting vortex breakdown domain curves are shown in figure 5 for the two shear-thinning fluids and a Newtonian fluid.

Escudier & Cullen (1996) observed the confined swirling flow of highly shear-thinning carboxymethylcellulose solutions for concentrations of 0.75–1.5% and with Reynolds numbers below  $Re = 174$ . The primary normal stress difference was measured, but the fluid was considered relatively inelastic because of low values in elasticity number ( $El < 0.002$ ). At all rotation rates examined, a vortex was observed on the disk which was dominated by inertia such that the secondary flow was in the ‘Newtonian’ direction and driven outwards along the rotating disk. However, a counter-rotating vortex was observed in the upper portion of the flow cell which was driven in the ‘reverse’ direction with a very slow secondary flow velocity and was near stagnant. An upward flowing jet of fluid containing a wavy structure was also present in several observations of Escudier & Cullen (1996) along the axis of symmetry.

A range of highly elastic shear-thinning polyacrylamide solutions (0.016–0.52%) were used by Hill (1969, 1972), in solvents of glycerol and water, to examine the effect of elasticity in swirling flow. ‘Reverse’ flow occurred for highly elastic liquids at low Reynolds number where the secondary flow is inwards along the rotating lid against centrifugal forces, upwards along the central axis away from the rotating disk and then along the outside stationary walls, as depicted in figure 6(a). At higher levels of Reynolds number and lower values of elasticity number, complex flow patterns were observed where an inertially driven ‘ring’ vortex forms at the edge of the rotating disk,

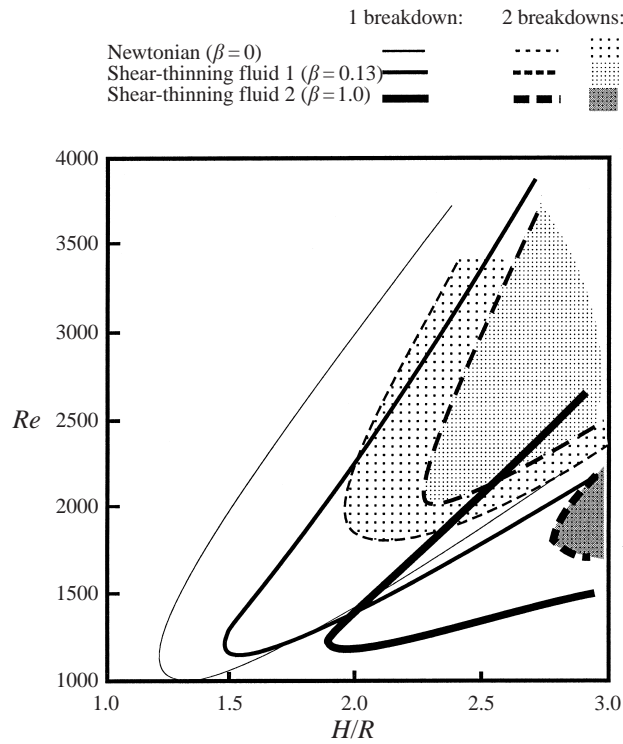


FIGURE 5. Comparison of the existence domain of vortex breakdown by Böhme *et al.* (1992) between a Newtonian fluid and two shear-thinning fluids.

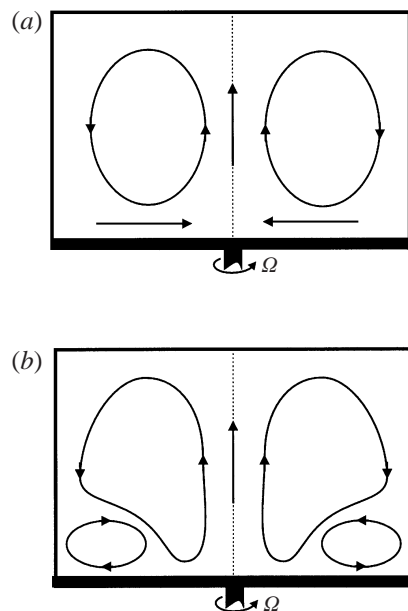


FIGURE 6. Secondary flow patterns observed by Hill (1972) for shear-thinning elastic liquids showing: (a) 'reverse' or elasticity driven flow; (b) counter-rotating vortices with an inertia-driven ring vortex located on the outside of the rotating lid. (a) is also predicted by Kramer & Johnson (1972) using a second-order fluid with  $El = 0.5$ .

counter-rotating with the main 'reverse' flow vortex structure, as shown in figure 6(b). Further increases in disk speed caused the growth of the outer edge vortex and then a highly unsteady flow. For low concentrations of polymer (0.03%), Hill (1972) also observed that the secondary flow transformed from 'reverse' flow at low Reynolds number to 'Newtonian-like' flow at high Reynolds number. Hill (1972) only observed 'Newtonian-like' flow without any apparent elastic behaviour for concentrations of polyacrylamide of 0.015%. The tangential and radial velocities were also measured for one highly elastic liquid in the 'reverse' flow state.

Day *et al.* (1996) used a highly elastic shear-thinning polyacrylamide solution (2.5% in water) and observed 'reverse' secondary flow at low Reynolds number. On increasing the Reynolds number, Day *et al.* (1996) observed the formation of a ring vortex on the centre of the disk and an instability where the core of the main vortex is observed to spiral with the primary motion of the fluid and is the same as the elastic instability shown in Part 2.

Numerical methods have been used in an attempt to predict the flow patterns observed for non-Newtonian fluids in confined swirling flow for both elastic and inelastic fluids. The constitutive equations used by Böhme *et al.* (1992) and Escudier & Cullen (1996) described inelastic fluids while those used by Kramer (1969) and Kramer & Johnson (1972), Nirschl & Stewart (1984), and more recently by Chiao & Chang (1990), described elastic fluids.

Böhme *et al.* (1992) performed a finite-element simulation and used a generalized Newtonian model in order to model only the shear-thinning viscosity of the fluids he used in his experiments which were mentioned previously for high-Reynolds-number flow. Vortex breakdown was predicted numerically with reasonable accuracy, but with some departure from the size and location of the initial breakdown bubble observed experimentally. Böhme *et al.* (1992) associated the deviations between the experiments and numerical prediction as possibly being due to the elasticity of the fluid, which was not considered in the constitutive equation used. Escudier & Cullen (1996) used the commercial computational fluid dynamics package 'Polyflow' with the shear-thinning viscosity described using a generalized Newtonian model which did not take into account fluid elasticity. The numerical model predicted only 'Newtonian-like' flow governing the whole flow cell and did not predict the counter-rotating vortices observed in the experiments.

Kramer (1969) and Kramer & Johnson (1972) were the first to try and predict the effect of elasticity in confined swirling flow and hence reproduce the experimental observations made by Hill (1972). Kramer & Johnson (1972) used a perturbation theory for a weak secondary flow superimposed on an arbitrary primary flow using both a second-order fluid model, which assumes a constant viscosity and a constant primary normal stress coefficient, and the WJFLMB constitutive model of Spriggs, Huppler & Bird (1966), which assumes a power law form of material functions but does not account for fluid memory. Figures 6(a) and 7 show the qualitative observations made by Kramer & Johnson (1972) when they used the second-order fluid model for constant Reynolds number and varied the normal stress coefficient, which equated to a variation in the elasticity number of between  $El = 0$  and  $El = 0.5$ . As the elasticity number was increased from  $El = 0$  to  $El = 0.0125$ , a small elastically driven vortex formed on the outer edge of the rotating disk in an otherwise Newtonian flow field (figure 7a). The elastic vortex then governed a majority of the flow field with a further increase in elasticity number to  $El = 0.025$ , while only a small inertial vortex remained on the centre of the rotating disk (figure 7b). 'Reverse' flow was then predicted with an increase in elasticity number to  $El = 0.5$  and elastic effects fully

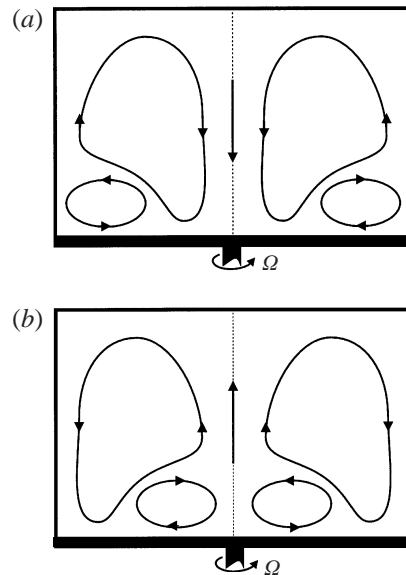


FIGURE 7. Secondary flow patterns predicted by Kramer & Johnson (1972) for a constant-viscosity second-order fluid with (a)  $El = 0.0125$  and (b)  $El = 0.025$ .

dominated (figure 6a). The predictions using the second-order fluid model did not qualitatively represent the observations of Hill (1972) except for the fully ‘reverse’ flow situation, although this is not surprising considering the simplicity of the model and its inability to represent the fluid rheology. The second-order model was also found to be highly inaccurate when comparing the analytical velocity measurements with those made by Hill (1972). However, the WJFLMB model, which was capable of representing the shear rheology of the fluid such as the variation in relaxation time and viscosity with shear rate, was found to predict the tangential and radial velocity profiles with reasonable accuracy for the case when ‘reverse’ flow is observed at low Reynolds number.

A global spectral method was used by Chiao & Chang (1990) while an orthogonal collocation method was used by Nirschl & Stewart (1984) with both methods applying the Criminale–Ericksen–Filbey (CEF) constitutive equation in an attempt to predict the observations of Hill (1972). The CEF equation is similar to the second-order model except that Chiao & Chang (1990) and Nirschl & Stewart (1984) use the Carreau A model (Carreau 1968) to describe the variations of the material properties with shear rate for the fluids of Hill (1972). Chiao & Chang (1990) found that the CEF model had some physical limitations and was a mathematical obstacle due to the third-order terms in the equation. Difficulties with the CEF model include its inability to describe fluid memory, and the fact that it generally only performs well for viscometric flows while the torsionally driven cavity produces non-viscometric flows. Also, Tanner (1985) recommended that the CEF constitutive model should be avoided outside of viscometric flows because its numerical predictions are prone to convergence problems. Therefore, the CEF model is not an appropriate model to use for predicting the behaviour of fluids in the torsionally driven cavity except for the purpose of examining the qualitative effects of elasticity and shear-thinning.

Both Nirschl & Stewart (1984) and Chiao & Chang (1990) were able to predict ‘reverse’ flow in many of the cases where Hill (1972) observed it experimentally.

Also, the numerical tangential and radial velocity profiles compared very well to the measurements of Hill (1972) for a ‘reverse’ flow situation. Chiao & Chang (1990) were able to predict a counter-rotating inertially driven vortex on the outer edge of the disk (figure 6b) for several of the cases when it was observed experimentally by Hill (1972). Contrary to the experiments of Hill (1972), Nirschl & Stewart (1984) did not predict an inertial vortex on the edge of the disk. Instead, their model predicted that an inertial vortex would form on the centre of the rotating disk, as did the model of Kramer & Johnson (1972) at moderate values of elasticity number (figure 7b). In addition, Chiao & Chang (1990) predicted a region of temporal instabilities and chaotic flow which were believed to be consistent with some of the observations made by Hill (1972) at high Reynolds number.

Wüsch & Böhme (1996) used a single-integral constitutive equation (Wagner model) to simulate their own experimental results for a shear-thinning elastic polyacrylamide solution. Although limited details were presented, the flow patterns were found to be similar to those observed by Hill (1972). Wüsch & Böhme (1996) state that the observed flow behaviour was qualitatively predicted when the Weissenberg number was altered for a set Reynolds number.

The open cylinder with rotating bottom lid was used experimentally for a shear-thinning elastic liquid (25% polyacrylamide (PAA) in water) and a constant-viscosity elastic liquid (silicon oil) by Böhme, Voss & Warnecke (1985). ‘Reverse’ flow was observed at low Reynolds number ( $Re < 0.013$  for 2.5% PAA) and a bulge in the free surface was produced which depended on the primary normal stress difference. The effect was termed the *Quelleffekt* because the fluid flowed upwards along the axis of symmetry as a source or *Quell*. Böhme *et al.* (1985) developed a second-order theory assuming a sufficiently slow flow and solved it using a numerical finite-element method. The results for the surface bulge size agreed well between experiment and the numerical analysis. It was found that the zero-shear rate normal stress coefficients could be determined by measuring the displacement of the free surface, and that the surface tension of the fluid had an insignificant influence on the result. It was also found that the axial bulge deformation was quadratic in the angular velocity of the rotating disk for low angular velocities. Debbaut & Hocq (1992) used the Oldroyd-B and Johnson–Segalman constitutive models to predict the bulge shape observed by Böhme *et al.* (1985). Both models assume a constant-viscosity for the test fluid and a quadratic dependence of the primary normal stress with shear rate. The second normal stress difference is predicted to be zero for the Oldroyd-B model, but it is quantified in the Johnson–Segalman equation such that the relative importance of the primary and second normal stress differences on the surface bulge could be examined. The surface bulge was found to be larger using the Oldroyd-B model, indicating that the primary normal stress difference caused the free surface to rise while the second normal stress difference acted against the first normal stress difference as far as the bulge shape was concerned. Good quantitative agreement on surface displacement was found between the predictions of Debbaut & Hocq (1992) and the experiments by Böhme *et al.* (1985). However, Siginer (1991) found that surface tension was important when measuring surface deformation to yield normal stress coefficients. In addition, Siginer (1991) predicted sectional streamline patterns with various sets of counter-rotating vortices observed which were dependent on the elasticity of the fluid and cylinder aspect ratio.

All previous experimental investigations on the confined swirling flow of non-Newtonian fluids have been performed using shear-thinning elastic liquids, although in some cases the elasticity was considered negligible. When the relaxation time has been

determined for the various fluids, it has also been invariably shear-rate dependent. Both the Reynolds number and the Weissenberg number were consequently evaluated using the zero shear-rate value of viscosity and with a shear-rate dependent relaxation time, respectively. This is despite the fact that the lid may be rotating at substantial rates, and that the magnitudes of the material properties vary throughout the flow cell. Comparison between different experiments and fluids has been difficult owing to the inability of the Reynolds number, Weissenberg number (or elasticity number) and a shear-thinning parameter to characterize the flow field. If the fluid is shear-thinning, then it is difficult to distinguish between the effects of shear thinning and those of elasticity, especially when the Reynolds number is high. Consequently, it is difficult to ascertain the role of elasticity in all of the above-mentioned observations. Also, prediction of the flow field for non-Newtonian fluids has not been able to produce all the observations made by Hill (1972) because of the limitations in the constitutive equations used and/or in the rheological data presented by Hill (1972). However, some good comparisons between experiments and numerical results were found for the case of 'reverse' flow of Hill's (1972) most elastic fluid. Numerical prediction in confined swirling flow is possible, but there is a need for experimental results using well-characterized fluids which can be described by more sophisticated constitutive models than those that have been used previously.

In the present work, the effects of elasticity are isolated by examining the confined swirling flow of a collection of constant-viscosity elastic liquids (Boger fluids) which may be considered as 'ideal' fluids. This paper, Part 1, investigates the behaviour of a set of low-viscosity Boger fluids containing up to 75 p.p.m. of either flexible polymer (polyacrylamide) or semi-rigid polymer (xanthan gum) when the flow field is dominated by inertia. The effect of the polymer, and hence slight fluid elasticity, on the existence domain for vortex breakdown will be examined. Part 2 will use medium to high-viscosity Boger fluids where the inertia is decreased until the flow field is fully dominated by fluid elasticity and viscosity. All the fluids are well characterized such that material functions required for various constitutive models may be determined. In particular, the polyacrylamide Boger fluids are ideal for use in the Oldroyd-B constitutive model because it requires a constant viscosity and a constant relaxation time. Radial and axial velocities are measured using particle image velocimetry (PIV) with particular emphasis placed on reporting and comparing the axial velocity profiles along or near the axis of symmetry. It is envisaged that the results presented will be ideal for comparison to numerical predictions in confined swirling flow and will allow testing of constitutive models and numerical techniques for steady and unsteady flows of viscoelastic fluids.

### 3. Experimental

The following section describes the confined swirling flow experiment and the techniques used to measure and visualize the secondary flow field.

#### 3.1. Apparatus

The experimental apparatus, as shown in figure 8 and also described by Day *et al.* (1996), consisted of an acrylic cylinder with radius  $70 \pm 0.25$  mm, situated in a rectangular acrylic water bath, with dimensions  $402 \times 402 \times 592$  mm<sup>3</sup>, to reduce image distortion effects. The bottom lid of the cylinder was a stainless steel disk which was rotated using a three-phase a.c. motor via a v-belt and pulley arrangement with a selectable reduction gearbox for the lower disk speed range. The rotation rate of

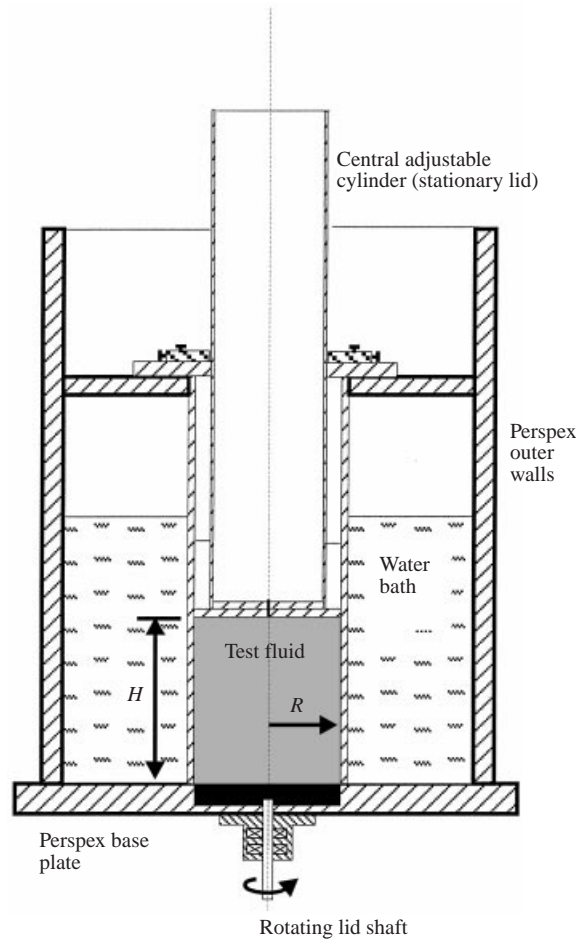


FIGURE 8. Torsionally driven cavity experimental rig.

the disk was controlled using a variable frequency unit connected to the a.c. motor, and was measured using a frequency counter with a resolution of approximately  $\pm 0.002 \text{ s}^{-1}$ . The stationary top lid was movable and lockable, and positioned according to the height to radius ratio required to within  $\pm 0.5 \text{ mm}$ . Both disk and cylinder were designed and built to ensure axial symmetry with the disk rotating with a lateral tolerance of  $\pm 50 \mu\text{m}$ .

Various top lids could be used which depended on the viscosity of the fluid such that air bubble entrainment was minimized as the lids were lowered into the fluid and set in place. A lid with one central small capillary hold (0.5 mm diameter), connected to a needle and a 1 mm diameter tube for dye insertion, was used for fluids with a low viscosity ( $\eta < 1.5 \text{ Pa s}$ ) and it also contained a flush mounted thermocouple. An alternative lid with 5 small holes (1 mm diameter) arranged regularly in a line across the lid surface was used for medium-viscosity fluids ( $1.5 < \eta < 3 \text{ Pa s}$ ). A third lid with a central small hole (1 mm diameter) and an off-centre large diameter hole ( $\approx 10 \text{ mm}$  diameter), was used for high-viscosity fluids ( $\eta > 3 \text{ Pa s}$ ) such that once the lid was lowered into the fluid, a large flat plug screw could be used to block the hole. Subsequent flow measurements showed that no detectable asymmetries in the flow field were present for any of the three lids.

During a given experiment, the temperature of the working fluid was found to increase owing to viscous heating, especially at high rotation rates and for viscous liquids. Therefore, to control the heating effects, the bath water was circulated through an Haake F3 environmental controller such that most experiments were conducted between 20 °C and 21 °C. For the lids without a flush mounted thermocouple, a thermocouple probe could be inserted through the capillary holes in the lids, or alternatively, for continual measurement it could sit in the capillary holes just outside the flow cell. The temperature of the test fluid was regularly measured to within  $\pm 0.05$  °C such that the governing dimensionless numbers could be determined accurately by taking into consideration temperature variation of the material functions.

### 3.2. Flow visualization

Illumination of the secondary flow plane was performed using a Coherent Highlight argon-ion laser, operating at 0.5 W, piped through an optical fibre to a cylindrical lens. This lens produced a multiline blue-green laser light sheet with a thickness of 1–2 mm. Dye flow visualization was conducted in order to observe ‘streaklines’ by dissolving fluorescein powder ( $\approx 0.2$  g l<sup>-1</sup>) into a small quantity of the test fluid. The dye was then added via either a syringe-tube-needle arrangement in the centre of the stationary lid for low-viscosity fluids, or by a syringe-tube-capillary arrangement in the other lids.

Colour photography of the dye streaklines was typically performed at an exposure of  $\frac{1}{4}$ – $\frac{1}{2}$  s and aperture  $f2$  to  $f4$ , using a 35 mm SLR camera with a noct-Nikkor 58 mm lens and 1BUV filter with EPP 100 ISO film. Images were slightly distorted in the radial direction such that the equivalent radial image distance was 108% of the actual distance at the edge of the field. Video imaging was performed using a Sony Hi8 video camera (model DXC537P) with a zoom lens.

### 3.3. Particle image velocimetry

Velocity data in the secondary flow plane was obtained using the two-dimensional optical technique of PIV (Pickering & Halliwell 1985; Adrian 1991). A similar technique, laser speckle velocimetry (LSV), has also been used previously by Binnington, Troup & Boger (1983) to obtain velocity profiles for Boger fluids. PIV was used in preference to the alternative measurement technique laser-Doppler anemometry (LDA) (Durst, Lehmann & Tropea 1981) owing to the prohibitively long acquisition periods that would be required for LDA when measuring the higher viscosity flows where in some cases fluid velocities were less than 1 mm s<sup>-1</sup>.

The following will briefly describe the PIV system which was based on simple multiple exposure photography for imaging and digital autocorrelation techniques for data processing (Adrian 1991; Meinhart, Prasad & Adrian 1993). A detailed description of the PIV system can be found in Stokes (1998).

The PIV images were recorded using a pulsed light source from either a 12-sided rotating mirror system as described by Gray *et al.* (1991) and shown in figure 9, or a mechanical shutter with light sheet optics. In both cases a 0.5 W argon ion laser light source was used with a fibre optic delivery and collimation lens. The flow was seeded using fluorescent rhodamine particles. A Nikon F4 camera with a noct-Nikkor 58 mm f1.2 lens was used to record the images onto 35 mm Kodak Tmax400 (TMY) film. The 35 mm transparencies were then digitized into 8 bit greyscale images at a resolution of 2700 d.p.i. by using a Polaroid SprintScan 35 scanner. The processing of images was carried out using autocorrelation and post-processing software developed by N.J.L. The software was set up to vary the size of the d.c. peak mask in the

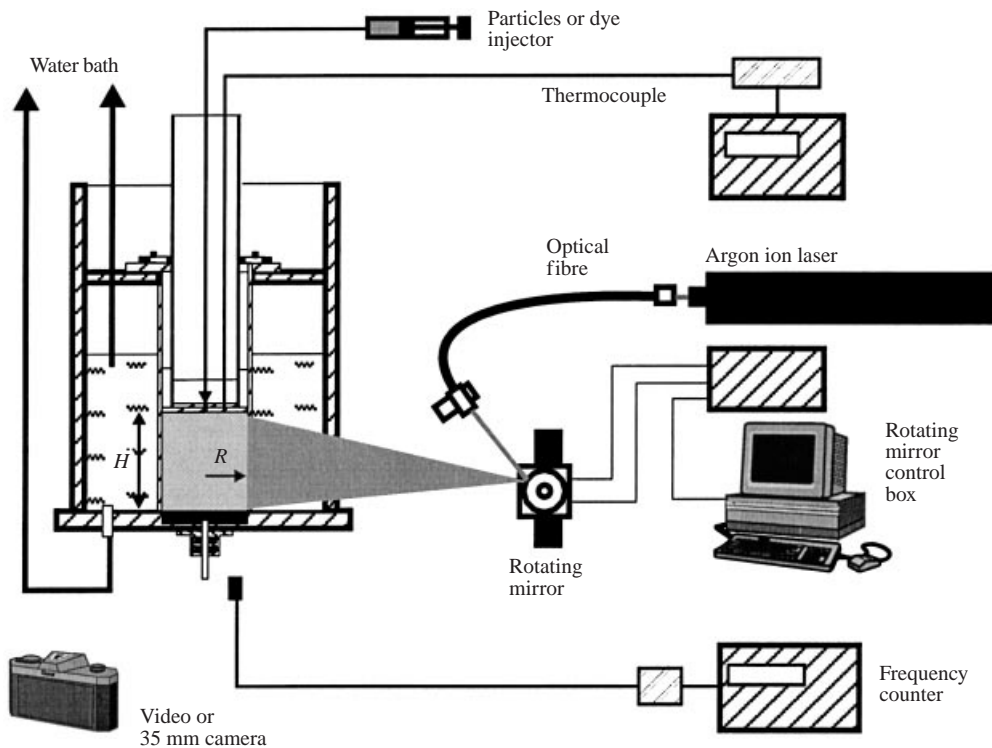


FIGURE 9. Torsionally driven cavity experimental set-up showing rotating mirror used for PIV studies.

correlation plane so that it was proportional to the particle image diameter (Lawson, Coupland & Halliwell 1997).

Figure 10 shows a typical PIV image with corresponding vector map and streamline plot. The two-dimensional PIV vector maps are measurements of velocity in the axial and radial plane. From this data, a predictor-corrector integration algorithm in the commercial software package of 'Tecplot' was used to obtain streamline traces. It should be noted, however, that because of the three-dimensional nature of the flow field, the streamlines in the following analysis are representative of the 'instantaneous' flow in the cross-plane and are termed 'sectional streamline patterns' (Perry & Steiner 1987).

As mentioned previously, the flow field is highly three-dimensional and contains a strong out-of-plane component, termed the azimuthal velocity ( $V_\theta$ ). In the worst case, this component will displace particles out of the light sheet between exposures causing data dropout in the vector map. Therefore, areas near the outer surfaces and, in particular, near the rotating disk, were found to have the greatest dropout and only the central region near the axis of symmetry contained reliable data, where the out-of-plane velocity component was lower. This problem was partly overcome by recording several PIV images with different pulse separations and then combining the sets of validated data. However, in the case where the secondary flow velocity was the same order of magnitude as or greater than the azimuthal velocity component, the majority of PIV vectors were obtained. Other errors were also generated around the axis of symmetry when particles were displaced across the centre with the primary

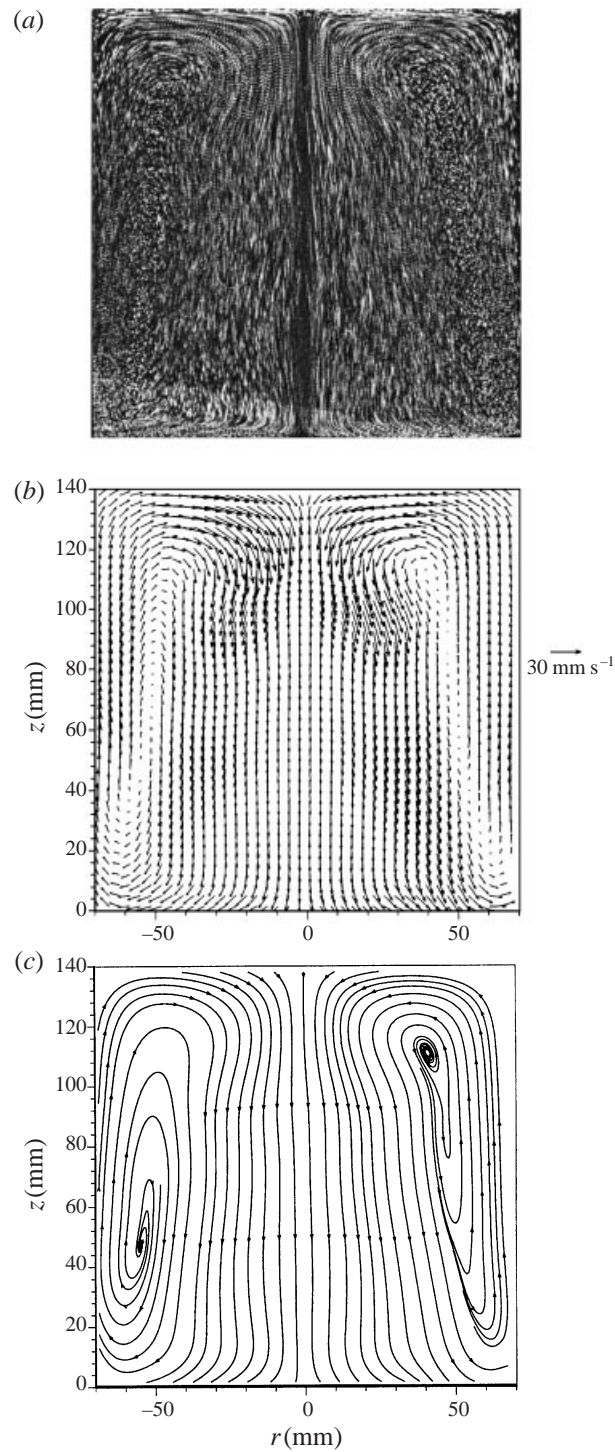


FIGURE 10. Secondary flow field for 75 p.p.m. polyacrylamide Boger fluid at  $Re = 2100$ ,  $We = 0.7$ , and  $H/R = 2$  showing: (a) PIV image; (b) vector map; (c) sectional streamline patterns.

flow due to either an excessive laser sheet thickness, high velocities in the primary flow and/or misalignment of the laser sheet position.

The measured radial and axial velocities, given the symbols  $V_r$  and  $V_z$ , respectively, are made dimensionless for comparative purposes by dividing by a characteristic velocity. The characteristic velocity is chosen to be the maximum azimuthal velocity ( $V_{\theta(max)} = 2\pi\Omega R$ ) in the system which is located at the edge of the rotating disk. The coordinate system is taken as  $(r, \theta, z)$  with  $r = 0$  and  $z = 0$  corresponding to the centre of the rotating disk. Therefore, a positive axial velocity corresponds to the fluid flowing upwards, vortically away from the rotating disk. The azimuthal component of vorticity ( $\omega_\theta$ ) was determined from the measured velocity data using the following definition:

$$\omega_\theta = \frac{\partial v_r}{\partial v_z} - \frac{\partial v_z}{\partial v_r}. \quad (7)$$

Components of the rate of strain tensor which could be determined are  $\dot{\gamma}_{rz}, \dot{\gamma}_{zr}, \dot{\gamma}_{rr}, \dot{\gamma}_{\theta\theta}, \dot{\gamma}_{zz}$ . Only  $\dot{\gamma}_{zz}$ , was used here to give an indication of the strain rate along axial streamlines about the central axis and was defined by  $\dot{\gamma}_{zz} = 2\partial v_z/\partial z$ .

#### 3.4. Error analysis

For the PIV system, the velocity vector  $V$  at any grid point is calculated from a calibrated magnification  $M$ , a particle image displacement  $\Delta s$  and a pulse separation  $\Delta t$  such that:

$$V = \frac{\Delta s}{M\Delta t}. \quad (8)$$

Therefore, if the uncertainty in measurement of the quantities  $M$ ,  $\Delta s$  and  $\Delta t$  is represented by the percentage errors  $\delta(M)$ ,  $\delta(\Delta s)$  and  $\delta(\Delta t)$ , respectively, then the total percentage error in velocity measurement,  $\delta(V)$  can be found from:

$$\delta(V) = \sqrt{[\delta(M)]^2 + [\delta(\Delta s)]^2 + [\delta(\Delta t)]^2}. \quad (9)$$

The magnification  $M$  (pixels  $\text{mm}^{-1}$ ) was estimated from known image dimensions such as the height and diameter of the flow cell, and the error was typically one pixel in 1000 or  $\delta(M) = 0.1\%$ . The maximum deviation in the mirror speed was noted as 3 r.p.m. in 167 r.p.m., resulting in a maximum pulse separation error of  $\delta(\Delta t) = 1.8\%$ . For the error in particle image displacement  $\delta(\Delta s)$ , previous work by Keane & Adrian (1991) is used to estimate the error from *a priori* information on the flow. *A priori* velocity information is required since the particle displacement error is strongly dependent on spatial velocity gradients (Keane & Adrian 1991) with the worst error occurring in the region of highest spatial gradient. From previous work (Lugt & Abboud 1987), the maximum gradient has been predicted at the edge and towards the centreline of the flow, and is of the order of  $10 \text{ mm s}^{-1}$  across a given interrogation region of size 1.3 mm. Therefore, with a mean particle image size of  $100 \mu\text{m}$  and a magnification of  $M = 0.15$ , the error in particle displacement is estimated to be in the range  $2.5\% < \delta(\Delta s) < 19.5\%$  for a corresponding range of pulse separations  $15 \text{ ms} < \Delta t < 143 \text{ ms}$ . The total error in measurement from equation (9) will then equal  $3.1\% < \delta(V) < 19.6\%$ . This estimate indicates that it is desirable to keep the laser pulse separation to a minimum owing to the errors generated by velocity gradients. Unfortunately, at lower pulse separations the lower range of secondary flow velocities cannot be resolved owing to insufficient particle image separations. Hence, a number of PIV vector maps were taken for a given flow with different pulse separations and the different sets of validated vectors combined. This technique allows the user to

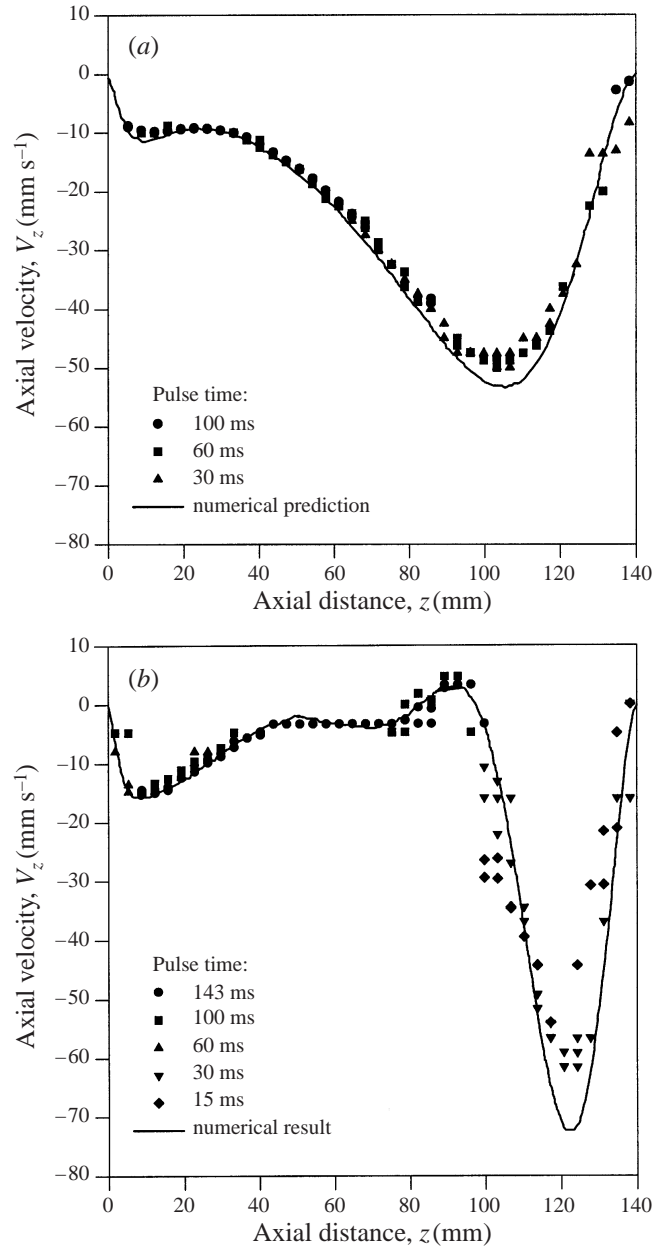


FIGURE 11. Comparison of the axial velocity along the centreline ( $r \approx 0$ ) measured using PIV and that predicted by Lugt & Abboud (1987) for the Newtonian solvent at (a)  $Re = 1000$ , (b)  $Re = 1500$ .

restrict the total error in measurement to  $\delta(V) < 10\%$  and also permits tuning of the data to account for the out-of-plane effects mentioned previously. Any remaining non-valid vectors can then be interpolated and the complete map smoothed to remove correlation noise.

A comparison is shown in figure 11 between PIV experimental measurements of the centreline axial velocity and those predicted using the numerical model of Lugt & Abboud (1987) for a Newtonian fluid at Reynolds numbers of  $Re \approx 1000$  and

$Re \approx 1500$ . Each plot shows axial velocities which were determined using a range of pulse separation times of between 15 ms and 143 ms. The experimental results compare well to the predicted measurements across the entire length of the cylinder. Deviations of around 10% between the experimental measurements and those predicted were found at the minimum peak in axial velocity, about which the velocity gradients were highest. This deviation matches the level of accuracy predicted in the previous error analysis and thus gives a sufficient degree of confidence in the technique for the following study of centreline flow fields.

#### 4. Rheology of test fluids

The following section includes a rheological description of the low-viscosity Boger fluids used in this study. The material parameters for several constitutive models are listed and a comparison is made between the measured and predicted linear viscoelastic properties. This analysis is necessary to enable the prediction of the flow behaviour of the fluids used in this study using numerical models.

##### 4.1. Test fluids

The test polymers used were a commercial grade of polyacrylamide (PAA) Separan AP30 (supplied by Dow Chemical Ltd, USA) and xanthan gum Keltrol (supplied by Kelco, Division of Merck & Co. Inc.). Polyacrylamide (AP30) is a flexible polyelectrolyte molecule with an average molecular weight ( $M_w$ ) reported in the literature to be between  $2 \times 10^6$  and  $4 \times 10^6$  (Eisenbrand & Goddard 1982; Lawlar *et al.* 1986; Tam & Tiu 1989*a, b*). Xanthan gum (Keltrol) is regarded as a semi-rigid polyelectrolyte molecule with a molecular weight reported to be between  $2 \times 10^6$  and  $7 \times 10^6$  (Holdzwarth 1978; Zirnsak 1995; Paradossi & Brant 1982; Norton *et al.* 1984; Sato, Norisuye & Fujita 1984).

The average molecular weights of the polymers were determined using size exclusion chromatography (SEC) with a multi-angle laser light scattering instrument (model: DAWN F, Wyatt Technology Corp.) and a differential refractometer (model: Waters 410) used as on-line detectors. Solutions of  $1 \text{ g l}^{-1}$  of polymer in 0.1 M sodium nitrate were filtered through  $0.45 \mu\text{m}$  Millipore filters before being passed through a series of Waters Ultrahydrogel (hydroxylated polymethacrylate based gel) SEM columns with  $250 \text{ \AA}$  and  $2000 \text{ \AA}$  pore size at a flow rate of  $0.8 \text{ ml min}^{-1}$ . The SEM columns separate each solution into components of different molecular weight. The electrolyte was used to minimise electrostatic interactions that may occur between the solute and the column surface.

The average molecular weight of polyacrylamide AP30 was measured as  $3.1 \times 10^6 \pm 0.04$  with a polydispersity ( $M_w/M_n$ ) of  $1.1 \pm 0.1$ , while the average molecular weight for xanthan gum Keltrol is  $6.3 \times 10^6 \pm 0.3$  with a polydispersity of  $1.2 \pm 0.2$ .

The low-viscosity Boger fluids were made using a solvent of 76 wt% glycerol–water and 0.02 wt% sodium azide with either 25, 45 and 75 p.p.m. of polyacrylamide or 25, 45 and 75 p.p.m. of xanthan gum. The solvent was kept constant such that the polymer had essentially the same conformation for all concentrations. The glycerol was technical grade (98%), purchased from Ajax Chemicals Pty Ltd, while the deionised water was obtained from a Millipore Milli-RO<sup>®</sup>4 water purification system which used 10 and  $3 \mu\text{m}$  pre-filters, a  $10 \mu\text{m}$  carbon filter, and a polyamide reverse osmosis unit. The water typically had a conductivity of  $2\text{--}8 \mu\text{S cm}^{-1}$  and pH ranging from 5.8 to 6.8. All polymer solutions were prepared by first dissolving the appropriate amount of polymer into deionised water to make a stock solution with a polymer

Polymer solution	$R_h$ (nm)	$L$ (nm)
45 p.p.m. PAA	43	—
75 p.p.m. PAA	37	—
45 p.p.m. XG	85	944
75 p.p.m. XG	123	1475

TABLE 2. PCS measurements of hydrodynamic size of polymers in 76% glycerol.

concentration of 0.1 wt%. The water was warmed to about 30–40 °C and the polymer was added gradually to the water while continually swirling the container in order to disperse the polymer and avoid agglomeration. Sodium azide was added to the stock solution (< 0.02 wt%) to act as a biocide. The stock solutions were placed on a roller mixer device at very low rotation rates for 12–48 h and, once the polymer was fully dissolved, the solutions were stored in the refrigerator. The experimental solutions were made by adding the appropriate amounts of polymer stock solution to the required glycerol and sodium azide with the balance made up with deionised water. The solutions were then mixed using a four-pronged impeller at low rotation rates for 8–12 h.

#### 4.2. Molecular properties and solution classification

The hydrodynamic size of each polymer in some of the solutions was determined using photon correlation spectroscopy (PCS) in a manner similar to that used by Ung *et al.* (1997). Further details of the technique and method used is found in Stokes (1998). The measurements for the hydrodynamic size of polyacrylamide and xanthan gum for concentrations of 45 p.p.m. and 75 p.p.m. in 76% glycerol–water are shown in table 2.

The length  $L$  of the xanthan gum molecule was determined using relations given by Broersma (1964) and Young *et al.* (1978) for rigid rod molecules as follows:

$$L = R_h \left( 2\sigma - 0.19 - \frac{8.24}{\sigma} + \frac{12}{\sigma^2} \right), \quad (10)$$

where  $\sigma = \ln(L/r)$  is the aspect ratio of a rod and  $r$  is the radius of the ‘rigid rod’. If  $r$  is assumed to be equal to about 2 nm, which is of the same order as that observed in the literature (Zirnsak 1995), then the length of the xanthan gum molecule ranges from 944 nm to 1475 nm with an aspect ratio of 472 to 738 for concentrations of 45 p.p.m. and 75 p.p.m., respectively.

The intrinsic viscosity was determined for the set of polyacrylamide and xanthan gum solutions using viscosity measurements and an automated SCHOTT-GERÄTE AVS30 intrinsic viscometer using Type 531-10 Ubbelohde viscometer ( $\dot{\gamma}_w < 40 \text{ s}^{-1}$ ) and the viscosity measured using rheometry which will be discussed later. The intrinsic viscosity in 76% glycerol was  $3.71 \text{ g}^{-1}$  for the polyacrylamide solutions and  $8.21 \text{ g}^{-1}$  for the xanthan gum solutions (Stokes 1998).

The polymer solutions are regarded as dilute when there is no interaction between molecules. A standard method used to evaluate whether a polymer solution is dilute is to determine a dimensionless concentration of polymer which can be given by either  $[\eta]c$  (Flory 1960) or  $cN_A V/M_w$  (Doi & Edwards 1986) where  $c$  is the polymer concentration,  $N_A$  is Avogadro’s number, and  $V$  is the volume occupied by a polymer molecule. Flexible polymers tend to occupy a spherical region in solution such that  $V = \frac{4}{3}\pi R_h^3$ . In the case of rigid molecules, the spherical region required such that the

large aspect ratio molecule can freely rotate without interaction with its neighbours is calculated from the molecule length such that  $V = \frac{1}{6}\pi L^3$ . The polymer solution is then regarded as dilute when the dimensionless concentration is less than unity.

The dimensionless concentrations for the 75 p.p.m. polyacrylamide solution were  $[\eta]c = 0.28$  and  $cN_A V/M_w = 0.005$  and, hence, all the polyacrylamide solutions were considered truly dilute using both the criteria of Flory (1960) and Doi & Edwards (1986), respectively. However, for the rigid xanthan gum solution,  $[\eta]c = 0.6$  while  $cN_A V/M_w \gg 1$ , and hence the two criteria are in conflict. Following the criteria of Doi & Edwards (1986), the xanthan gum solutions are considered semi-dilute.

### 4.3. Rheology

Steady shear and dynamic property measurements were made using a Carri-Med CSL100 rheometer with a 6 cm diameter plate and 1' 59" cone angle, and a Contraves Low-Shear 40 rheometer equipped with a cup and bob system. The main cup and bob system used with the Contraves was the MS 41S/1S which consisted of a 5.5 mm radius bob with an effective length of 8 mm situated in a 6 mm radius cylinder (cup). The Contraves rheometer, which has a high sensitivity and is designed specifically for low-viscosity fluids (Tam & Tiu 1989*b*), was used to measure the properties of the low-viscosity Boger fluids independently. This was performed by the rheology group at Nanyang University, Singapore, headed by K. C. Tam. An attempt was made to measure the primary normal stress difference using a Weissenberg R19 rheometer but this was found to be too low to measure. An opposed jet apparatus, the Rheometrics RFX, was used to measure an apparent extensional viscosity.

The Carri-Med rheometer was only capable of measuring the viscosity of the low-viscosity Boger fluids for shear rates above about  $1\text{--}2\text{ s}^{-1}$ , below which the viscosity measurement was unreliable. The Carri-Med results must be treated with some caution for fluids of low viscosity because it measures a higher viscosity than expected at low shear rates, even for Newtonian fluids, such that an otherwise constant-viscosity fluid appears to be shear-thinning (Lee & Sexton 1994; Stokes 1998). The Contraves rheometer was capable of reliably determining the viscosity of the low-viscosity Boger fluids for shear rates above  $0.1\text{ s}^{-1}$ . The viscosity measured using both rheometers is shown as a function of shear rate in figures 12(*a*) and 12(*b*) for the polyacrylamide and xanthan gum low-viscosity Boger fluids, respectively, at  $20^\circ\text{C}$ . The Carri-Med results are distinguished by using dotted symbols, and the Newtonian solvent is shown only as a straight line for clarity. The measurements from the two rheometers overlap to within a few per cent. Figure 12(*a*) indicates that each polyacrylamide solution has a constant viscosity which is such that there is a linear relationship between the shear stress and shear rate. The behaviour of the xanthan gum solutions, shown in figure 12(*b*), indicates the presence of slightly shear-thinning viscosity with a deviation from a linear shear stress–shear rate relationship. However, for the 75 p.p.m. xanthan gum solution which was regarded as the most shear-thinning, the zero shear-rate viscosity was only a factor of two above the infinite shear-rate viscosity and the slope (power-law exponent) of the shear stress–shear rate curve was only 0.92. The shear thinning parameter was determined using equation (6) to be  $\beta = 0.00014$  by fitting the viscosity data to the master curve of Böhme *et al.* (1992). Therefore, in comparison to the fluids used by Böhme *et al.* (1992), the fluids used in this work can all be considered to have a constant viscosity. The low shear rate value of viscosity was used as the viscosity of all solutions and the results are summarized in table 3.

The dynamic properties of the low-viscosity Boger fluids were too low to be reliably measured using the Carri-Med rheometer (Lee & Sexton 1994; Stokes 1998). However,

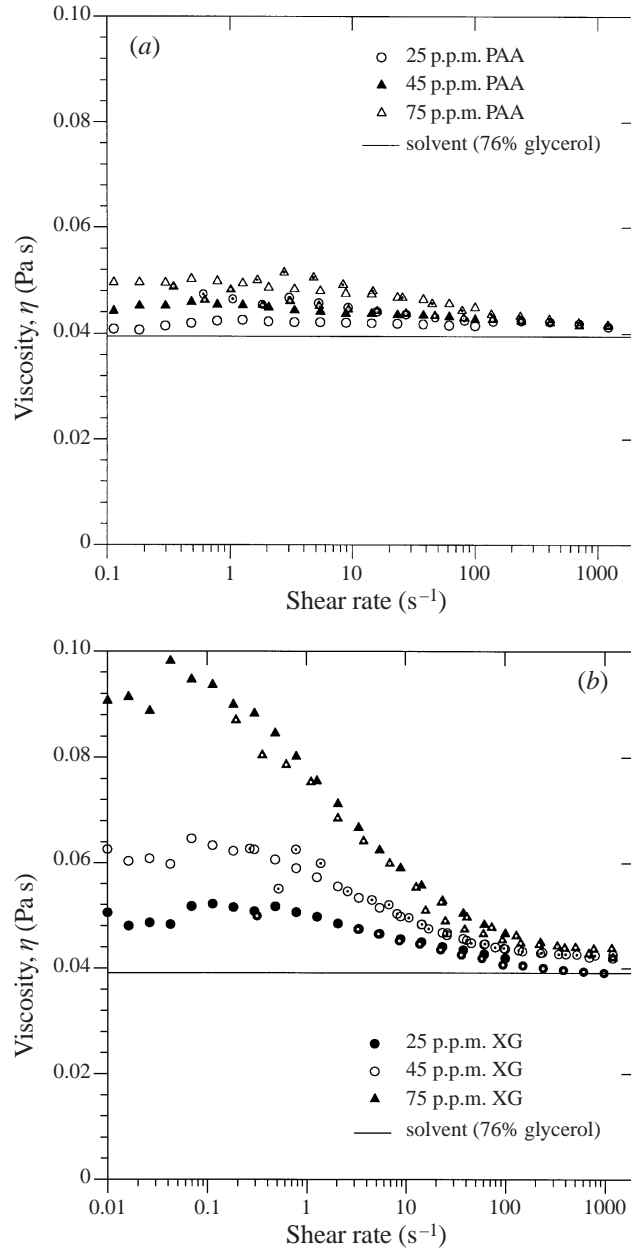


FIGURE 12. Steady shear properties for (a) the low-viscosity polyacrylamide Boger fluids and (b) the low-viscosity xanthan gum Boger fluids, using the Contraves LS40 and Carri-Med CSL100 rheometers. Dotted symbols are those measurements obtained from the Carri-Med.

through the use of the Contraves rheometer which has greater sensitivity, the dynamic properties for the low-viscosity Boger fluids could be measured. The results for the storage modulus ( $G'$ ) and dynamic viscosity ( $\eta'$ ) as a function of frequency ( $\omega$ ) are shown in figures 13(a) and 13(b) for the polyacrylamide and xanthan gum Boger fluids, respectively. The storage modulus for the Newtonian solvent was too low to reliably measure (Stokes 1998). The dynamic property measurements for the polymer

Polymer concentration (p.p.m.)	$\eta_0$ (mPa s)	Consistency factor $K$ (mPa s <sup>n</sup> )	Power law index $n$
Solvent	$39.5 \pm 0.5$	39.5	1
25 p.p.m. PAA	$41 \pm 1$	40.7	1
45 p.p.m. PAA	$46 \pm 1$	43.1	1
75 p.p.m. PAA	$50 \pm 1$	47.4	1
25 p.p.m. XG	$51 \pm 1$	47.8	0.9806
45 p.p.m. XG	$63 \pm 2$	55.1	0.9575
75 p.p.m. XG	$95 \pm 5$	72.3	0.9151

TABLE 3. Steady shear measurements for low-viscosity polyacrylamide and xanthan gum Boger fluids with their corresponding power law parameters indicated such that  $\eta = K\dot{\gamma}^{n-1}$ .

solutions were more reliable because the fluids contained some degree of elasticity. However, these measurements for the polymer solutions were also near the limitations of the instrument, and, in particular, the results for the polyacrylamide Boger fluids should be treated with some caution since there was only a minor dependence for  $G'$  on polymer concentration. However, different behaviour of the storage modulus with frequency was measured between the xanthan gum and polyacrylamide solutions, which was expected owing to their semi-rigid and flexible polymer conformations, respectively. Figure 13(a) shows that the storage modulus for the polyacrylamide Boger fluids has a quadratic dependence on frequency, which is expected for flexible polymer molecules at low frequencies. The dynamic viscosity, shown in figure 13(a) as dotted symbols, is similar to the shear viscosity, while the loss modulus is linear with frequency for the polyacrylamide Boger fluids. In figure 15, the storage modulus for the xanthan gum solutions are shown to vary linearly with frequency for the highest concentration (75 p.p.m.) and with  $\omega^{1.5}$  at the lowest concentration (25 p.p.m.). The dynamic viscosities for the xanthan solutions, indicated by dotted symbols in figure 13(b), were similar to the shear viscosities while the loss modulus marginally deviated from a linear dependency on frequency indicating slight shear-thinning behaviour. Similar frequency behaviour for the dynamic properties of the fluid used here has been observed previously at low frequencies for high-viscosity polyacrylamide and xanthan gum Boger fluids, as reviewed by Zirnsak (1995).

An opposed-jet apparatus, the Rheometrics RFX, was used to measure the behaviour of the low-viscosity Boger fluids due to extension. Details of the instrument and technique are well detailed in previous works by Fuller *et al.* (1987), Schunk, DeSantos & Scriven (1990), and Hermansky & Boger (1995). Polyacrylamide and xanthan gum in glycerol and water mixtures, which are similar to those in this work, were measured by Fuller *et al.* (1987). The opposed jet apparatus is not capable of producing a true uniaxial extensional flow field. The velocity field is not uniform across the nozzle face and therefore the extension rate is not constant with respect to radial or axial position such that it is unlikely that steady-state polymer conformations can be achieved. Therefore, in this case the extensional viscosity can only be regarded as an estimate and referred to as an apparent extensional viscosity. However, the opposed jet apparatus is currently the only known commercially available instrument which can differentiate between a low-viscosity fluid being elastic or inelastic.

The extensional properties, in the form of an apparent Trouton ratio ( $Tr = \eta_e/\eta$ ), for the low-viscosity polyacrylamide Boger fluids are shown in figure 14(a) using 1 mm

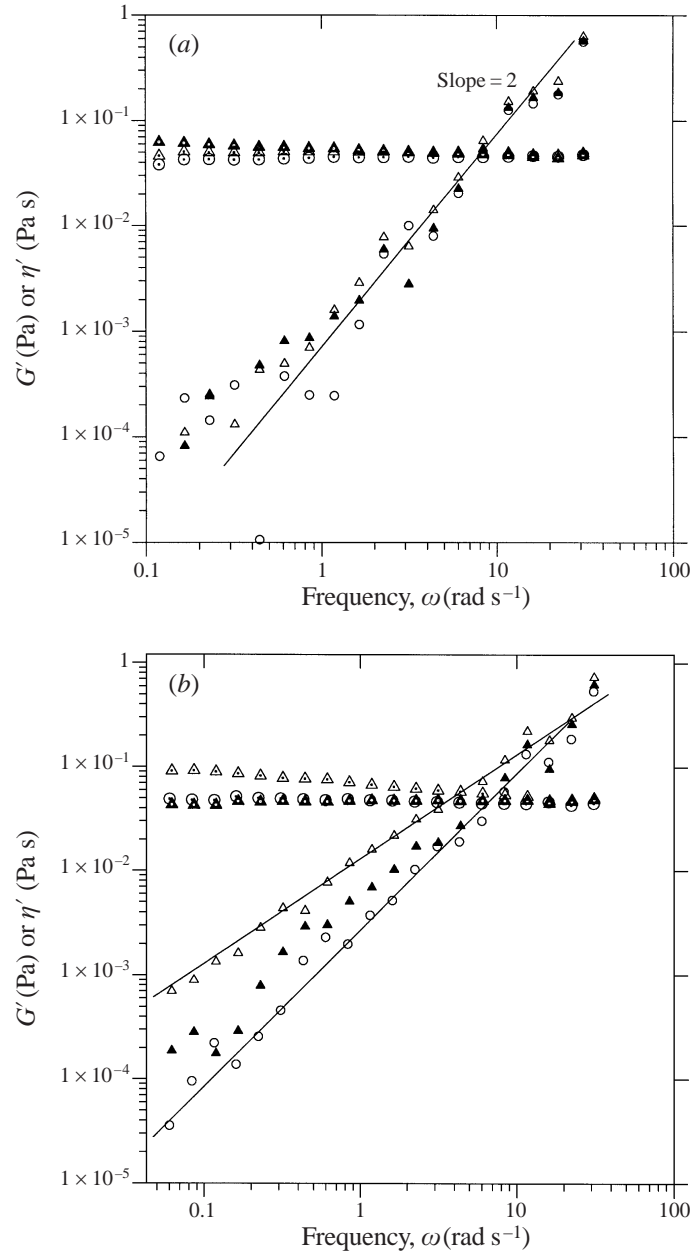


FIGURE 13. Linear viscoelastic properties for (a) the low-viscosity polyacrylamide Boger fluids and (b) the low-viscosity xanthan gum Boger fluids, using the Contraves LS40 rheometer showing the storage modulus  $G'$  and dynamic viscosity  $\eta'$  (dotted symbols).

diameter nozzles. The opposed jet apparatus was only capable of measuring a Trouton ratio of  $Tr \approx 4$  for the Newtonian solvent, and not the value of  $Tr = 3$  expected for a Newtonian fluid in a true uniaxial extensional flow field. The apparent Trouton ratio for the polyacrylamide Boger fluids is initially at a value of  $Tr \approx 4$  at low extension rates and then it increases to a maximum at extension rates of  $\dot{\epsilon} \approx 1000 \text{ s}^{-1}$ , after which the Trouton ratio decreases. The mechanisms for the apparent decrease

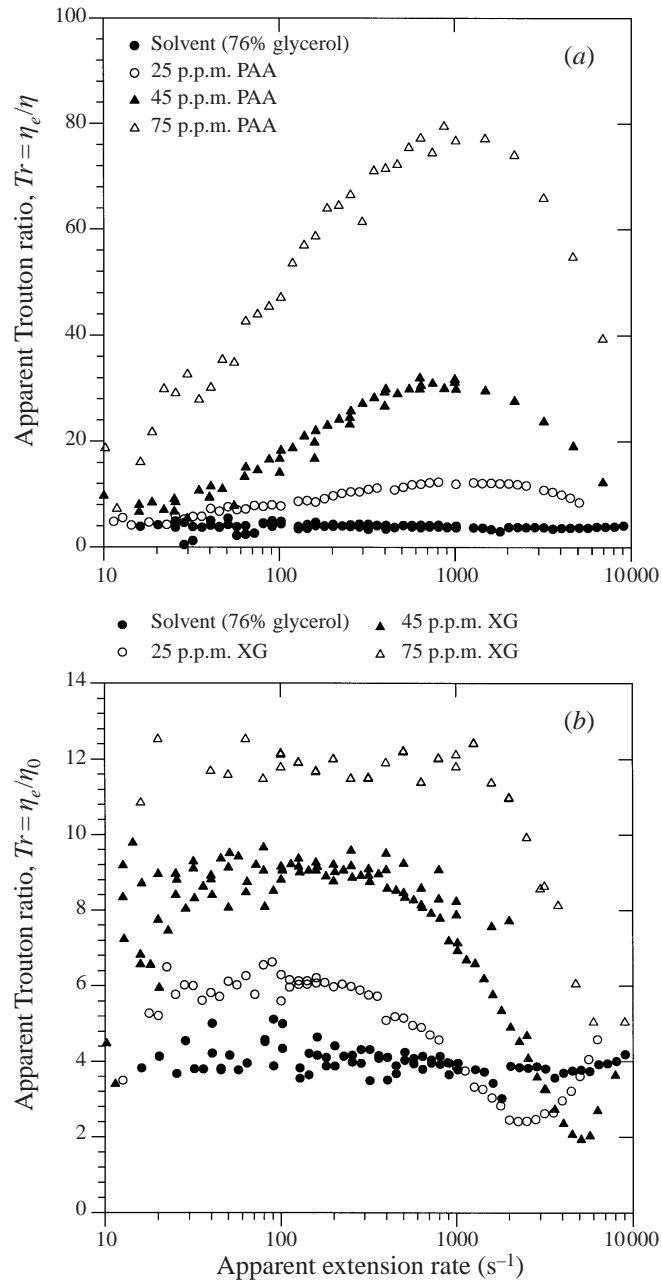


FIGURE 14. Extensional viscosity measurements using the Rheometrics RFX for (a) low-viscosity polyacrylamide Boger fluids and (b) for low-viscosity xanthan gum Boger fluids, and shown as an apparent Trouton ratio.

at high rates has not been well established, but may be associated with the polymer not having sufficient time to extend in the flow field, or it may be due to a flow instability. The general behaviour of the polyacrylamide solutions is that they are all extension rate thickening, which is a general characteristic for flexible polymers. The extension rate thickening behaviour was consistent across all concentrations, and may

Fluid	$\eta_0$ (Pa s)	$K_e$ (Pa s <sup><i>n</i></sup> )	$n_e$	Maximum <i>Tr</i>
Solvent	0.0395	0.16	1	4.05
25 p.p.m. PAA	0.041	0.0794	1.32	12
45 p.p.m. PAA	0.046	0.162	1.32	30
75 p.p.m. PAA	0.050	0.447	1.32	72
25 p.p.m. XG	0.051	0.265	1	6.1
45 p.p.m. XG	0.063	0.57	1	9.0
75 p.p.m. XG	0.095	1.11	1	12

TABLE 4. Extensional viscosity measurements for low-viscosity polyacrylamide and xanthan gum Boger fluids for  $10 < \dot{\epsilon} < 1000 \text{ s}^{-1}$  with the power law parameters indicated such that:  $\eta_e = K_e \dot{\epsilon}^{n_e-1}$ .

be expressed using a power law model. A summary of the extensional behaviour of polyacrylamide Boger fluids is indicated in table 4.

The apparent Trouton ratio for the xanthan gum Boger fluids is shown in figure 14(b) and is relatively constant for extension rates below  $\dot{\epsilon} \approx 1000 \text{ s}^{-1}$ , with a summary of the results indicated in table 4. The area of constant extensional viscosity is characteristic of rigid or semi-rigid macromolecules and with perfectly aligned rigid rods. Large-aspect-ratio macromolecules and rigid rods align instantaneously with the flow field, even at relatively low extension rates, such that the extensional viscosity is relatively independent of extension rate. The xanthan gum solutions, however, show extension rate thinning behaviour at high extension rates ( $\dot{\epsilon} > 1000 \text{ s}^{-1}$ ) which is similar to that observed for the polyacrylamide solutions. This decrease may mean that either the macromolecules do not have enough time to align in the flow field or there is a flow instability. At extreme extension rates, the apparent Trouton ratio rises again, but this is likely to be due to the anomalies in the instrument discussed previously.

The density was measured for the Newtonian solvent and polymer solutions using 25 ml calibrated density flasks and was determined to be  $\rho = 1196 \pm 2 \text{ kg m}^{-3}$  at  $20^\circ \text{C}$  for all solutions.

#### 4.4. Constitutive model parameters

The polymer relaxation time for several molecular constitutive theories may be estimated using the intrinsic viscosity (see Bird *et al.* 1987b). For example, the Oldroyd-B constitutive equation, which is suitable to use for the flexible polymers and hence for the polyacrylamide solutions, may be derived from the elastic dumbbell model with the following relation used to determine the longest relaxation time ( $\lambda_1$ ):

$$\lambda_1 = \frac{[\eta]\eta_s M_w}{R_g T} \quad (11)$$

where  $\eta_s$  is the solvent viscosity (Pa s),  $R_g$  is the universal gas constant ( $8.314 \text{ J K}^{-1} \text{ mol}^{-1}$ ), and  $T$  is the temperature (K). The retardation time ( $\lambda_2$ ) in the Oldroyd-B model is given by  $\lambda_2 = \lambda_1(\eta_s/\eta_0)$ . The relaxation time in the Maxwell constitutive model ( $\lambda_M$ ) is related to the Oldroyd characteristic times by:  $\lambda_M = \lambda_1 - \lambda_2$ . The longest Rouse and Zimm model relaxation times may also be determined, because the polymer solutions are dilute, by multiplying the Oldroyd-B relaxation time by the factors  $6\pi^2$  and  $0.423\pi^2$ , respectively. Therefore, characteristic relaxation times

Concentration of polymer	$\eta_0$ (mPa s)	$\lambda_1$ or $\lambda_D$ (s)	$\lambda_2$ (s)	$\lambda_M$ (s)	$El$
Solvent	39.5	—	—	—	—
25 p.p.m. PAA	41	0.186	0.179	0.007	$49 \times 10^{-6}$
45 p.p.m. PAA	46	0.186	0.160	0.026	$204 \times 10^{-6}$
75 p.p.m. PAA	50	0.186	0.147	0.039	$332 \times 10^{-6}$
25 p.p.m. XG	51	0.838	—	0.19	$1.65 \times 10^{-3}$
45 p.p.m. XG	63	0.838	—	0.31	$3.33 \times 10^{-3}$
75 p.p.m. XG	95	0.838	—	0.58	$9.4 \times 10^{-3}$

TABLE 5. Estimated material properties for the low-viscosity polyacrylamide and xanthan gum Boger fluids.

have been obtained for four constitutive models which are used to describe flexible molecules without the need for measurement of the primary normal stress difference or storage modulus. The viscosity, Oldroyd-B relaxation and retardation times, the Maxwell relaxation time, and the elasticity number are shown for the low-viscosity polyacrylamide Boger fluids in table 5. The Maxwell relaxation time is used as the characteristic time of the fluid when evaluating the Weissenberg and elasticity numbers for the fluids used in the torsionally driven cavity.

The validity of using the aforementioned models is demonstrated by predicting the linear viscoelastic properties using the relaxation times calculated from the intrinsic viscosity. A comparison between the predicted and measured reduced storage modulus ( $G'_R = G'M_w/cR_gT$ ) is shown in figure 15(a) as a function of the reduced frequency ( $\omega_R = \omega\lambda_1$ ). Only the values predicted for the 75 p.p.m. polyacrylamide solution are shown for clarity with the other concentrations behaving in a very similar manner. A prediction is also shown for the Rouse and Zimm models using data provided by Ferry (1980). All of the aforementioned models were able to predict the measured  $G'_R$  accurately at medium values of  $\omega_R$ . The measured  $G'_R$  deviates at low  $\omega_R$  because the measurements are near the limitations of the rheometer. The Oldroyd-B, Rouse and Zimm models fail to predict  $G'_R$  at high  $\omega_R$  whereas the Maxwell model performed well across the whole range of  $\omega_R$ . Therefore, the storage modulus for the low-viscosity polyacrylamide Boger fluids has been accurately predicted using the relaxation time calculated from intrinsic viscosity measurements.

An attempt was made to predict the extensional viscosity measurements using the Oldroyd-B and Maxwell models. The models both predict strain rate thickening behaviour, which is observed experimentally, but the predicted extensional viscosity asymptotes to infinity when  $\dot{\epsilon} = 1/(2\lambda)$ . The critical extension rate is therefore  $2.7 \text{ s}^{-1}$  and  $13 \text{ s}^{-1}$  for the Oldroyd-B and Maxwell model, respectively, for the 75 p.p.m. polyacrylamide Boger fluid, and therefore the models are incapable of describing the apparent extensional viscosity measured for the polyacrylamide solutions using the opposed jet apparatus. It also highlights the need to use these models only for flows where strain rates are low such that the extensional viscosity is finite.

The rigid-dumbbell constitutive model (see Bird *et al.* 1987b) may be used to describe rigid or semi-rigid molecules in solution and, hence, was considered appropriate to use for the xanthan gum solutions. The rigid-dumbbell model may use the same relation for the relaxation time ( $\lambda_D$ ) as that for the elastic dumbbell model, i.e.  $\lambda_D = \lambda_1$  where  $\lambda_1$  is given by (12). The rigid dumbbell relaxation time is displayed in table 5

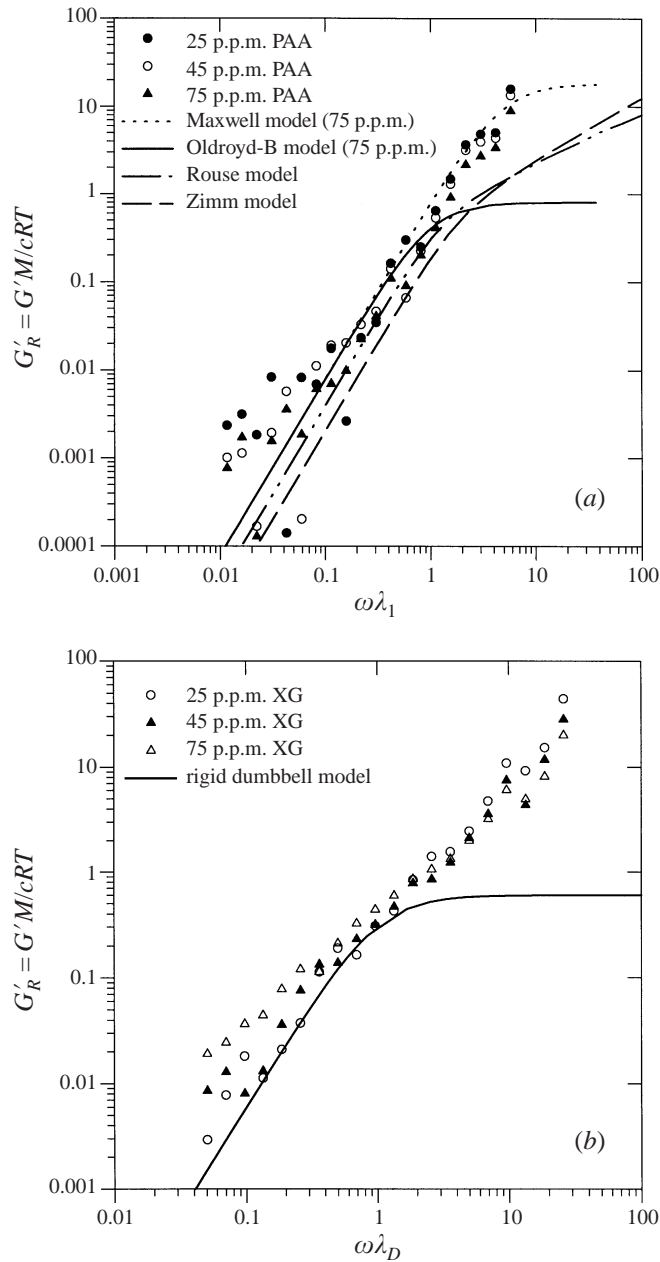


FIGURE 15. Comparison between the measured reduced storage modulus  $G'_R$  for (a) low-viscosity polyacrylamide Boger fluids and that predicted using selected constitutive models, and (b) the low-viscosity xanthan gum Boger fluids and that predicted using the rigid-dumbbell constitutive model; the relaxation time was calculated from intrinsic viscosity measurement.

for the xanthan gum solutions along with the corresponding Maxwell relaxation time, which was calculated in the same fashion as for the polyacrylamide Boger fluids.

The validity of using a rigid-dumbbell model to describe the low-viscosity xanthan gum Boger fluids was tested by comparing the measured values of  $G'_R$  with those predicted in figure 15(b). No concentration dependence for  $G'_R$  was predicted using

Concentration of xanthan gum (p.p.m.)	$\eta_0$ (mPa s)	$\eta_e$ (mPa s)	$\eta_e$ (RD) (mPa s)	$\eta_e$ (RR) (mPa s)
0	39.5	160	119	119
25	51	310	486	136
45	63	570	778	157
75	95	1110	1221	174

TABLE 6. Comparison of the apparent extensional viscosity measurements for the xanthan gum Boger fluids and those predicted from the rigid-dumbbell model (RD) of Bird *et al.* (1987b) and Batchelor's (1971) theory for semi-dilute perfectly aligned Rigid Rods (RR).

the rigid-dumbbell model. Very good agreement is found between the measured and the predicted  $G'_R$ , particularly at low concentrations of xanthan. As the concentration was increased, the measured  $G'_R$  deviates from those predicted as the slope of the measured  $G'_R$ - $\omega_R$  curve decreases. Therefore, deviation of the model from the actual measurements may be associated with a departure of the fluids from being a dilute solution such that as the concentration is raised there is increased interaction between molecules. At high frequency, the rigid-dumbbell model predicts a constant  $G'_R$  which is not observed experimentally.

The rigid-dumbbell model of Bird *et al.* (1987b) and Batchelor's theory for perfectly aligned rigid rods (Batchelor 1970, 1971), were used to predict the extensional behaviour of xanthan gum. The results (table 6) show that the rigid-dumbbell model predictions are in reasonable agreement with the measured extensional viscosity and, hence, the model is suitable for the description of the xanthan gum in extension.

In conclusion, the rheological properties of the low-viscosity Boger fluids used in this study can be predicted to within an order of magnitude of the experimental measurements using simple constitutive models such as the Oldroyd-B and rigid-dumbbell models. These models were considered reasonably accurate, considering that the fluids had a low viscosity and low elasticity. These constitutive models are therefore recommended for future analytical studies on the torsionally driven cavity flow of the viscoelastic fluids used in this work.

## 5. Results

Section 5.1 presents the results obtained using flow visualization and PIV for the test fluids comprised of 75 p.p.m. or less of polyacrylamide or xanthan gum polymer dissolved in a Newtonian 76% glycerol-water solvent. All fluids have an essentially constant viscosity such that the observed differences in flow behaviour from the Newtonian case are attributed to fluid elasticity associated with the presence of either the highly flexible polyacrylamide or the high-aspect-ratio rigid xanthan gum macromolecules. Flow-visualization images using fluorescent dye are initially shown for the 45 p.p.m. polyacrylamide solution for three sets of cylinder aspect ratios. Section 5.2 examines the effect of polymer, and hence elasticity, on the existence domain for vortex breakdown. Velocity measurements are shown in §5.3 to assist in the establishment of the possible reasons for a change in the flow behaviour which results from fluid elasticity and to provide quantitative data suitable for comparison with numerical studies.

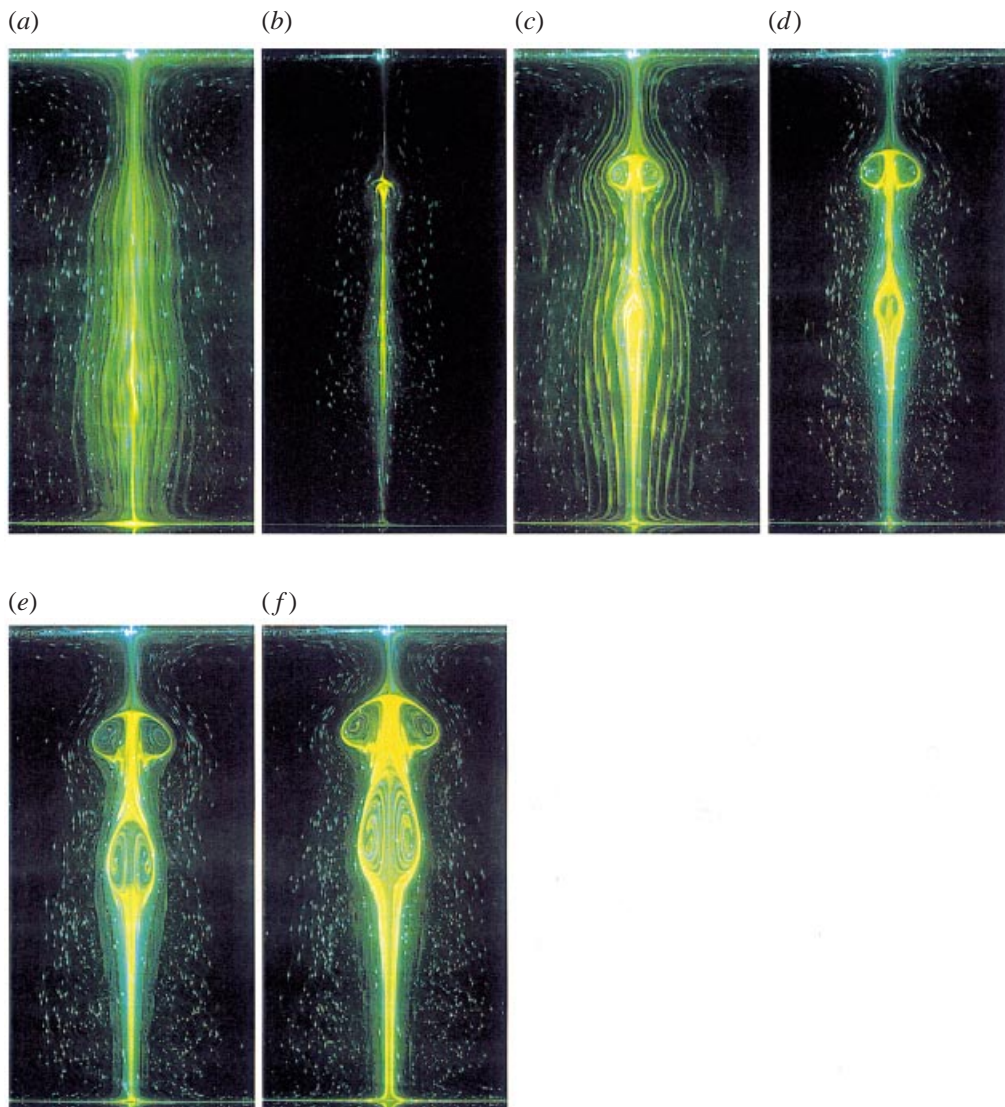


FIGURE 16. Flow visualization images for 45 p.p.m. polyacrylamide Boger fluid at  $H/R = 2.5$  for (a)  $Re = 2015$ ,  $We = 0.41$ , (b)  $Re = 2297$ ,  $We = 0.47$ , (c)  $Re = 2373$ ,  $We = 0.48$ , (d)  $Re = 2443$ ,  $We = 0.50$ , (e)  $Re = 2636$ ,  $We = 0.54$ , (f)  $Re = 2922$ ,  $We = 0.6$ .

### 5.1. Flow visualization

The flow visualization secondary flow patterns for 45 p.p.m. polyacrylamide are illustrated in figures 16, 17, and 18 for aspect ratios ( $H/R$ ) of 2.5, 2, and 1.5, respectively. Only the central portion of the secondary flow cell is shown, with corresponding dimensions of  $83.9 \times 175 \text{ mm}^2$ ,  $69.2 \times 140 \text{ mm}^2$ , and  $50.6 \times 105 \text{ mm}^2$  for a  $H/R$  of 2.5, 2 and 1.5, respectively, to illustrate the changing structure of the vortex core as breakdown occurs. The flow structures presented are visually similar to those observed and described by Escudier (1984) for a Newtonian liquid although the critical conditions for the occurrence of breakdown are altered owing to the influence of

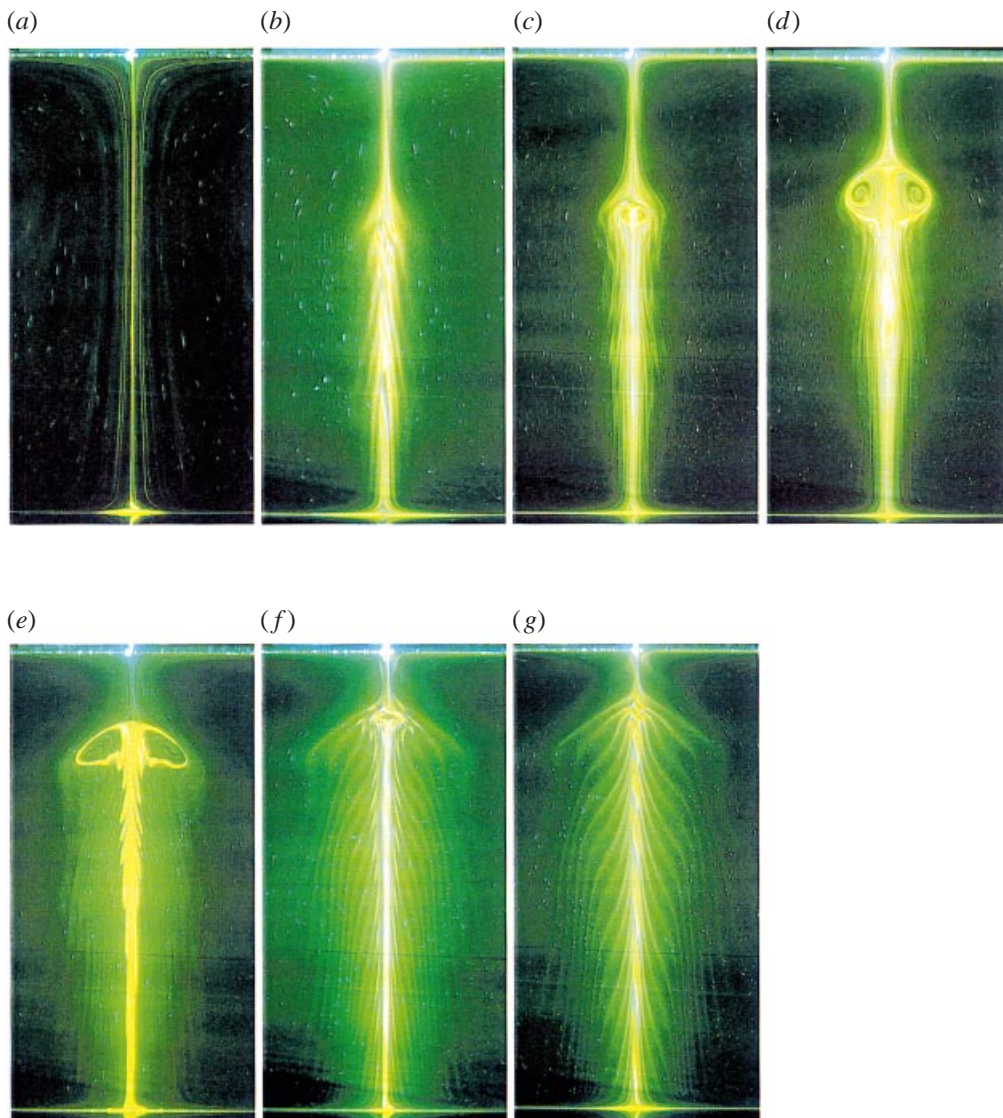


FIGURE 17. Flow visualization images for 45 p.p.m. polyacrylamide Boger fluid at  $H/R = 2$  for (a)  $Re = 1059$ ,  $We = 0.22$ , (b)  $Re = 1686$ ,  $We = 0.34$ , (c)  $Re = 1760$ ,  $We = 0.36$ , (d)  $Re = 1974$ ,  $We = 0.40$ , (e)  $Re = 3245$ ,  $We = 0.66$ , (f)  $Re = 3442$ ,  $We = 0.70$  (g)  $Re = 3625$ ,  $We = 0.74$ .

elasticity. The secondary flow for the polymer solution is also in the same direction as for a Newtonian fluid.

Figure 16 illustrates the secondary flow patterns for 45 p.p.m. polyacrylamide at an aspect ratio of  $H/R = 2.5$ . At low Reynolds numbers, a straight line of dye flows down the centreline into the Ekman boundary layer and is recirculated outwards along the rotating disk, up the sidewalls, along the stationary lid and down the central vortex core once again. However, as the Reynolds number is increased to  $Re = 2015$  (figure 16a), wavy dye streak lines are observed around the centreline, and what appears like a spiral on the centreline. A spiral of dye is usually observed at Reynolds numbers just below those required to cause breakdown and is an artefact

of flow visualization, and, therefore, should not be confused with an asymmetry in the flow (Hourigan, Graham & Thompson 1996). A stagnation point is produced upon increasing the Reynolds number to  $Re = 2300$  (figure 16*b*) which is an indicator of the incipient breakdown state. The stagnation point moves upstream once breakdown takes place and an adverse pressure gradient causes the production of a weakly flowing recirculation zone between two stagnation points. A single vortex breakdown bubble is clearly visible at a Reynolds number of  $Re = 2375$  (figure 16*c*). The flow can also be observed to decelerate just downstream from the bubble where a build-up of dye is shown. On subsequent increases in Reynolds number, another stagnation point occurs with the production of a second breakdown bubble, as shown for a Reynolds number of  $Re = 2445$  (figure 16*d*). Further increases in Reynolds number lead to increases in bubble size and a shift of the second bubble upstream towards the stationary lid, as shown in figure 16(*e*) and 16(*f*).

Figures 17 and 18 show the progress of the occurrence of a single vortex breakdown bubble for  $H/R = 2$  and  $H/R = 1.5$ , respectively, for 45 p.p.m. polyacrylamide. At  $H/R = 2$ , no second vortex breakdown bubble is observed using 45 p.p.m. polyacrylamide, although the second vortex breakdown bubble is observed for a Newtonian fluid. In both figures 17 and 18, the single breakdown bubble is observed to grow in size initially and then change shape as the Reynolds number is increased. Figure 17(*e*) and figure 18(*c*) show a flattening out of the bubble downstream near the stagnation point. As the Reynolds number is increased further, the stagnation point rises and ultimately vortex breakdown disappears, as shown in figure 17(*g*).

### 5.2. Existence domain of vortex breakdown

The steady-state existence domain of vortex breakdown, in terms of Reynolds number and aspect ratio, for the polyacrylamide and xanthan gum Boger fluids are shown in figures 19 and 20, respectively, at polymer concentrations of 0, 25 and 45 p.p.m. The solid lines in the diagrams represent the existence domain for the single upstream vortex breakdown bubble while the dashed lines represent the existence domain of the second vortex breakdown bubble. Upon increasing the rotation speed of the disk, the flow can become unsteady initially, but then return to a stable flow field after waiting several minutes. Therefore, it is difficult ascertaining the unsteady regime observed by Escudier (1984) for Newtonian fluids (see figure 3). Also, when a high disk rotation rate is maintained, severe viscous heating occurs where the temperature can increase by more than  $1^\circ\text{C}$  after only a couple of minutes, which subsequently causes the material properties to be altered. Therefore, the unsteady regime is not examined in the present work owing to the difficulties in ascertaining its existence domain combined with the adverse effects associated with viscous heating. The flow field beyond the upper limit of vortex breakdown is also not examined.

There is a shift in the existence domain of vortex breakdown for the polyacrylamide solutions to higher Reynolds number and aspect ratios owing to the influence of elasticity upon addition of flexible polymer to the Newtonian solvent. Figure 19 indicates that the degree of shift in the vortex breakdown is found to increase with polyacrylamide concentration. A greater Reynolds number is required for the appearance and disappearance of the first and second recirculation bubbles, at a constant aspect ratio, for the polyacrylamide solutions when compared to a Newtonian fluid. In the case of the 45 p.p.m. polyacrylamide Boger fluid, the critical Reynolds number required for breakdown is 20% larger than that required for a Newtonian fluid. Also, the minimum critical aspect ratio, below which vortex breakdown is not observed, increases with polyacrylamide concentration. In the case of the 45 p.p.m.

polyacrylamide Boger fluid when compared to the Newtonian solvent, the minimum critical aspect ratio for the first breakdown bubble increases by approximately 20%. However, the minimum critical aspect ratio for the second breakdown bubble increases by about the same absolute magnitude as that for the first breakdown bubble. The upper domain curves, where the single vortex breakdown bubble disappears, for each polyacrylamide concentration merge to a common curve and are offset at greater Reynolds numbers than for the Newtonian fluid. Vortex breakdown is not observed at all for 75 p.p.m. polyacrylamide for aspect ratios below  $H/R = 2.8$ .

The vortex breakdown existence domain is also altered by semi-rigid xanthan gum as shown for polymer concentrations of 25 and 45 p.p.m. in figure 20. The area bounded by the vortex breakdown domain curves decreases with increasing xanthan concentration and no second breakdown bubble is observed at aspect ratios below  $H/R = 2.5$  for the 45 p.p.m. xanthan gum. There is only a slight increase in the Reynolds numbers corresponding to the formation of the first breakdown bubble and a decrease in the Reynolds numbers corresponding to the disappearance of the first and second breakdown bubble with increasing xanthan concentration. This corresponds to about a 25% decrease in Reynolds numbers required for the disappearance of the first breakdown bubble for the 45 p.p.m. xanthan gum Boger fluid. There is also a small shift ( $\approx 5\%$ ) to higher Reynolds numbers for the occurrence of the second breakdown bubble for the 25 p.p.m. xanthan gum Boger fluid. The xanthan gum also causes the minimum critical aspect ratio required for breakdown to increase with polymer concentration to a high as about 40% for the 45 p.p.m. xanthan gum solution. Vortex breakdown is not observed for aspect ratios of less than  $H/R = 2.8$  for 75 p.p.m. xanthan gum.

It should be noted that the xanthan gum solutions are slightly shear-thinning above shear rates of  $\dot{\gamma} \approx 1\text{--}10\text{ s}^{-1}$ , while the Reynolds number is based on the zero shear-rate viscosity. For the overall flow kinematics, the degree of shear-thinning for the xanthan solutions is considered negligible when it is compared to the highly shear-thinning fluids of Böhme *et al.* (1992). The shear-thinning parameter for the 75 p.p.m. xanthan gum Boger fluid is  $\beta = 0.00014$ , whereas for the fluids of Böhme *et al.* (1992),  $\beta \geq 0.13$ . The major effect of shear-thinning in the experiments of Böhme *et al.* (1992) was to increase the minimum critical aspect ratio required for breakdown. Therefore, with values of the shear-thinning parameters close to zero, the slight shear-thinning behaviour of the xanthan gum Boger fluids will have no effect on the minimum critical aspect ratio required for breakdown. Hence, the only effect of the slight shear-thinning behaviour of the xanthan gum solutions is the difficulty associated with defining a viscosity to use in the Reynolds number. By defining the viscosity as the zero shear-rate value, the Reynolds number will be underestimated, considering that the flow kinematics are governed by shear rates above  $\dot{\gamma} \approx 1\text{ s}^{-1}$  since the rotation rate of the disk is generally greater than  $\Omega \approx 1\text{ s}^{-1}$ . If a lower viscosity is used to define the Reynolds number for the xanthan solutions, then the Reynolds number will be larger than those reported here. This causes the vortex breakdown domain curves for the xanthan gum solutions to be shifted to higher Reynolds numbers and therefore be similar to the domain curves for the polyacrylamide Boger fluids.

### 5.3. Velocity measurements

Particle image velocimetry has been used to determine the axial and radial velocity field in the secondary flow plane for the Newtonian solvent and the 45 and 75 p.p.m. polyacrylamide and xanthan gum Boger fluids. A typical vector field and sectional streamline plot for the 75 p.p.m. polyacrylamide Boger fluid is shown in figure 10

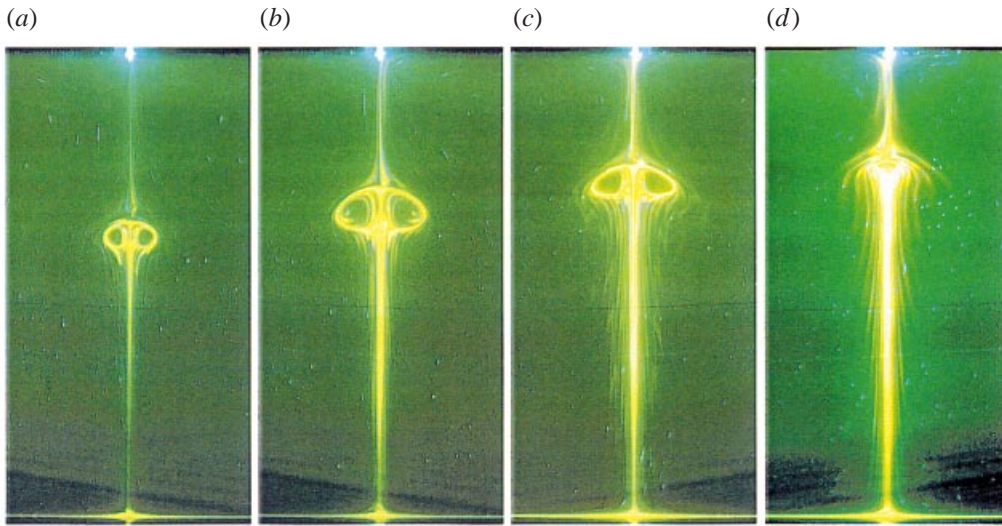


FIGURE 18. Flow visualization images for 45 p.p.m. polyacrylamide Boger fluid at  $H/R = 1.5$  for (a)  $Re = 1403$ ,  $We = 0.29$ , (b)  $Re = 1574$ ,  $We = 0.32$ , (c)  $Re = 1808$ ,  $We = 0.37$ , (d)  $Re = 1959$ ,  $We = 0.40$ .

for the case of a Reynolds number of  $Re = 2100$  and an aspect ratio of  $H/R = 2$ . At these conditions, vortex breakdown is observed for a Newtonian fluid but it is suppressed for the 75 p.p.m. polyacrylamide Boger fluid. The axial and radial velocity profiles are shown in figure 21 as contour plots where solid lines indicate a positive velocity while dashed lines indicate a negative velocity noting that the origin is located at the centre of the rotating disk. The velocity is constant along a contour line with the absolute velocity given alongside the diagrams.

The secondary flow for the 75 p.p.m. polyacrylamide Boger fluid is examined using the vector plot and velocity contour diagrams in figures 10 and 21, respectively. Starting from the origin in the middle of the rotating disk, fluid is quickly pumped outwards along the disk to the stationary sidewalls. The radial velocity (figure 21*b*) shown in the region closest to the disk is difficult to visualize, and, therefore, the velocity in this region is high in error, as discussed in §3.4. Fluid then flows upward along the stationary sidewall, with a peak in velocity of around  $-32 \text{ mm s}^{-1}$  (figure 21*a*), before turning inwards as it encounters the top stationary lid. The fluid then flows inwards along the stationary lid with a similar radial velocity to that present along the rotating disk (figure 21*b*). The fluid then flows down the central region where it passes through a peak in the axial velocity of more than  $32 \text{ mm s}^{-1}$  at a height of  $z = 120 \text{ mm}$  for a radius of  $r = \pm 15 \text{ mm s}^{-1}$  (figure 21*a*). The fluid then slows down as it moves down the central axis to a region of almost constant axial velocity for  $z < 100 \text{ mm}$  with  $-12 < V_z < -16 \text{ mm s}^{-1}$  before passing through another small peak at  $z \approx 15 \text{ mm}$ . The flow along the central core region is dominated by the axial velocity with only small radial fluctuations indicated at  $z \approx 100 \text{ mm}$ , which results from the divergence of the streamlines (figures 10 and 21*b*).

A contour diagram of the azimuthal component of vorticity is shown in figure 21(*c*) with a positive vorticity indicated as that directed into the page. In the left-hand half of figure 21(*c*), there is an area of negative azimuthal vorticity near the central axis which, according to Lopez (1990), is a necessary condition for vortex breakdown to

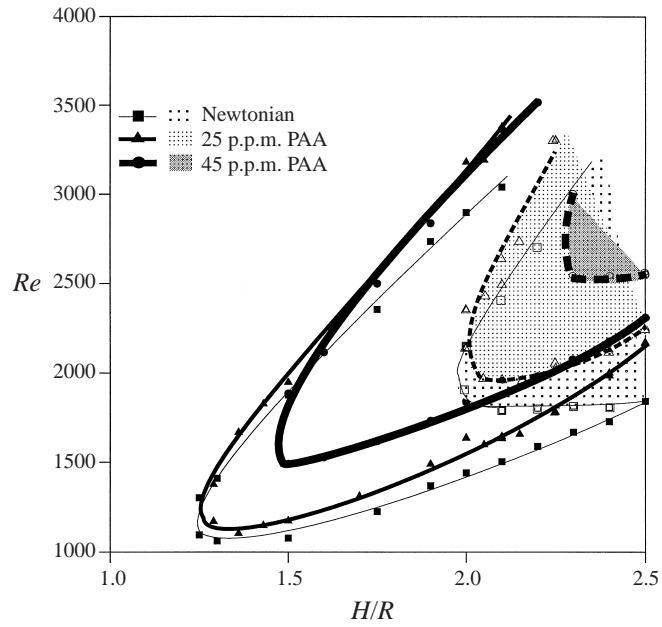


FIGURE 19. Existence domain for vortex breakdown of low-viscosity polyacrylamide Boger fluids and the Newtonian solvent (76% glycerol). Solid line and filled symbols: 1 breakdown. Dashed line, open symbols and shaded area: 2 breakdowns.

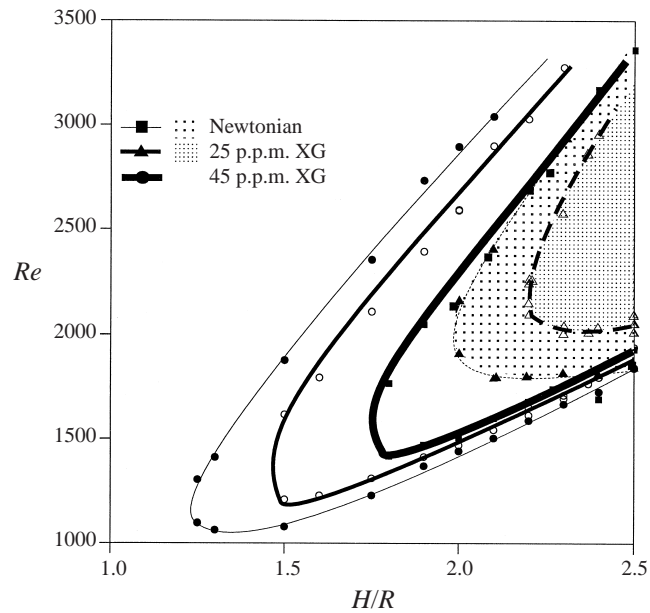


FIGURE 20. Existence domain for vortex breakdown of low-viscosity xanthan gum Boger fluids and the Newtonian solvent (76% glycerol). Solid line and filled symbols: 1 breakdown. Dashed line, open symbols and shaded area: 2 breakdowns.

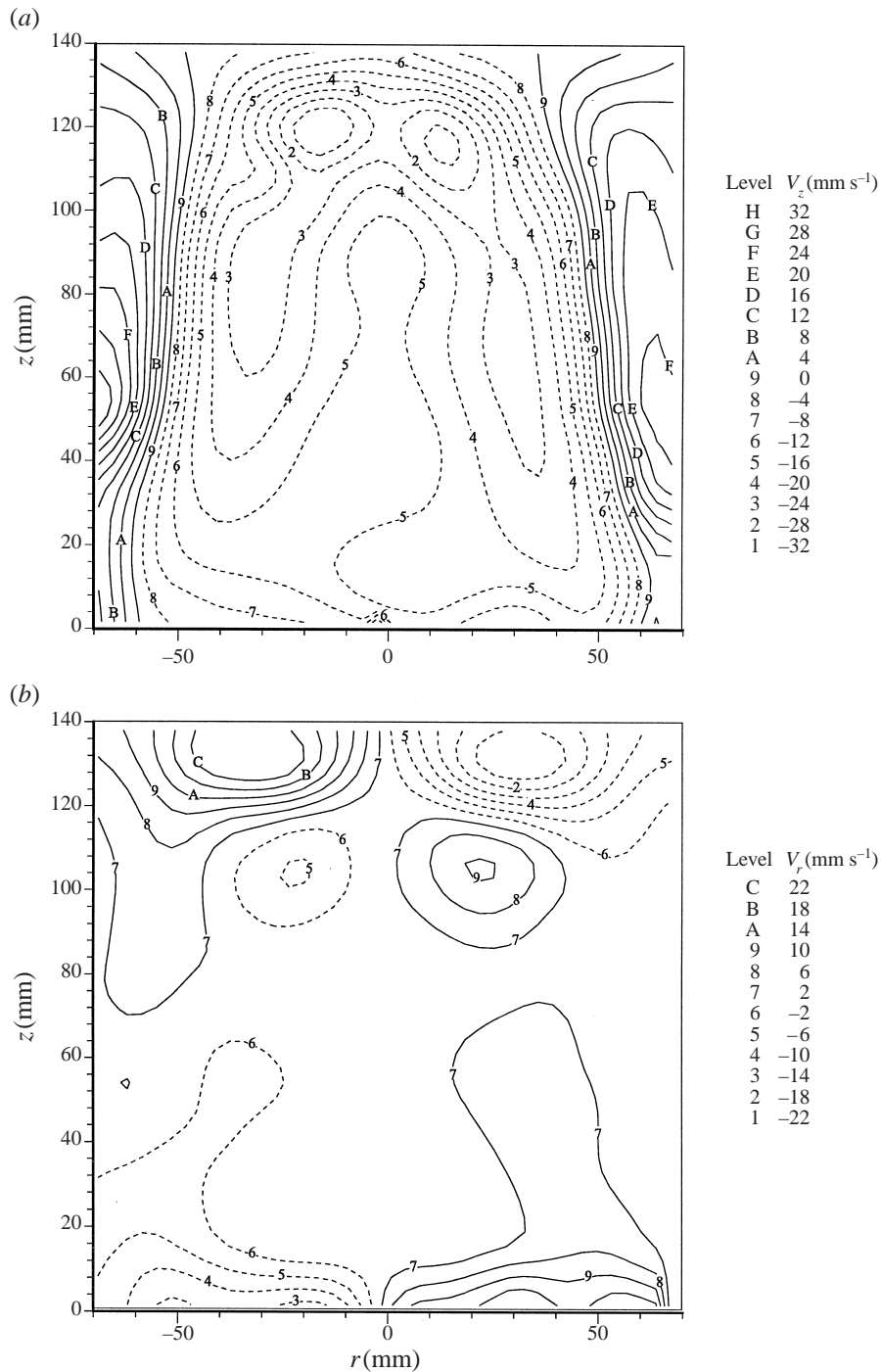


FIGURE 21 (a, b). For caption see facing page.

occur. The streamlines and vector plot in figure 10 indicate that the streamlines have a concave form, which is also considered a necessary condition before breakdown occurs. Yet, vortex breakdown is not observed at any Reynolds number at this aspect ratio for the 75 p.p.m. polyacrylamide Boger fluid which suggests that although the

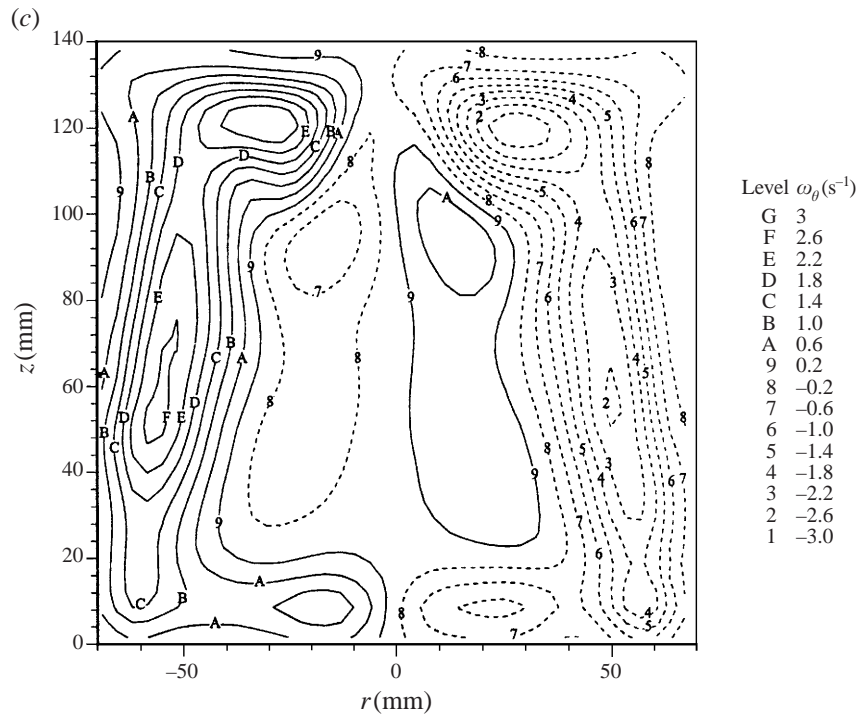


FIGURE 21. Flow field for 75 p.p.m. polyacrylamide Boger fluid at  $Re = 2100$ ,  $We = 0.7$ , and  $H/R = 2$  showing (a) axial velocity distribution, (b) radial velocity distribution, (c) azimuthal component of vorticity. Refer to figure 10 for corresponding vector field.

criteria of Lopez (1990) may be a necessary condition required for breakdown to occur, a negative azimuthal vorticity in the central core does not necessarily indicate that breakdown will occur.

The axial velocity close to the central axis where  $-5 \text{ mm} < r < 5 \text{ mm}$  is determined for each fluid, at various Reynolds numbers before and after breakdown, with the results shown for an aspect ratio of  $H/R = 2$  in figures 22(a)–22(e). The axial velocity is shown in dimensionless form by dividing by the maximum azimuthal velocity which corresponds to that produced at the edge of the rotating disk ( $2\pi R\Omega$ ). Lines shown on the diagrams represent lines which best fit the data. The rotating disk corresponds to  $z = 0$  such that a negative axial velocity indicates the fluid flowing towards the rotating disk.

The axial velocity distribution for the Newtonian fluid at an aspect ratio of  $H/R = 2$  in figure 22(a) is used to describe the axial flow profiles. Note that the first and second breakdown bubble occur for a Newtonian fluid with an aspect ratio of  $H/R = 2$  at  $Re \approx 1450$  and  $Re \approx 1800$ , respectively, with the second bubble disappearing at  $Re \approx 2300$ . No bubble is observed at all above  $Re \approx 3000$ . The axial velocity distribution initially has a minimum velocity just above the rotating lid at low Reynolds number with a narrow axial velocity distribution. As the Reynolds number is raised to  $Re = 380$ , the axial velocity distribution becomes broader and the minimum moves to a position further away from the rotating disk. At Reynolds numbers of  $Re > 990$ , the minimum axial velocity moves closer to the stationary disk and the magnitude in velocity just above the rotating disk is low. The axial velocity distribution becomes a narrow peak ( $1.1 < z/R < 2$ ) with the minimum

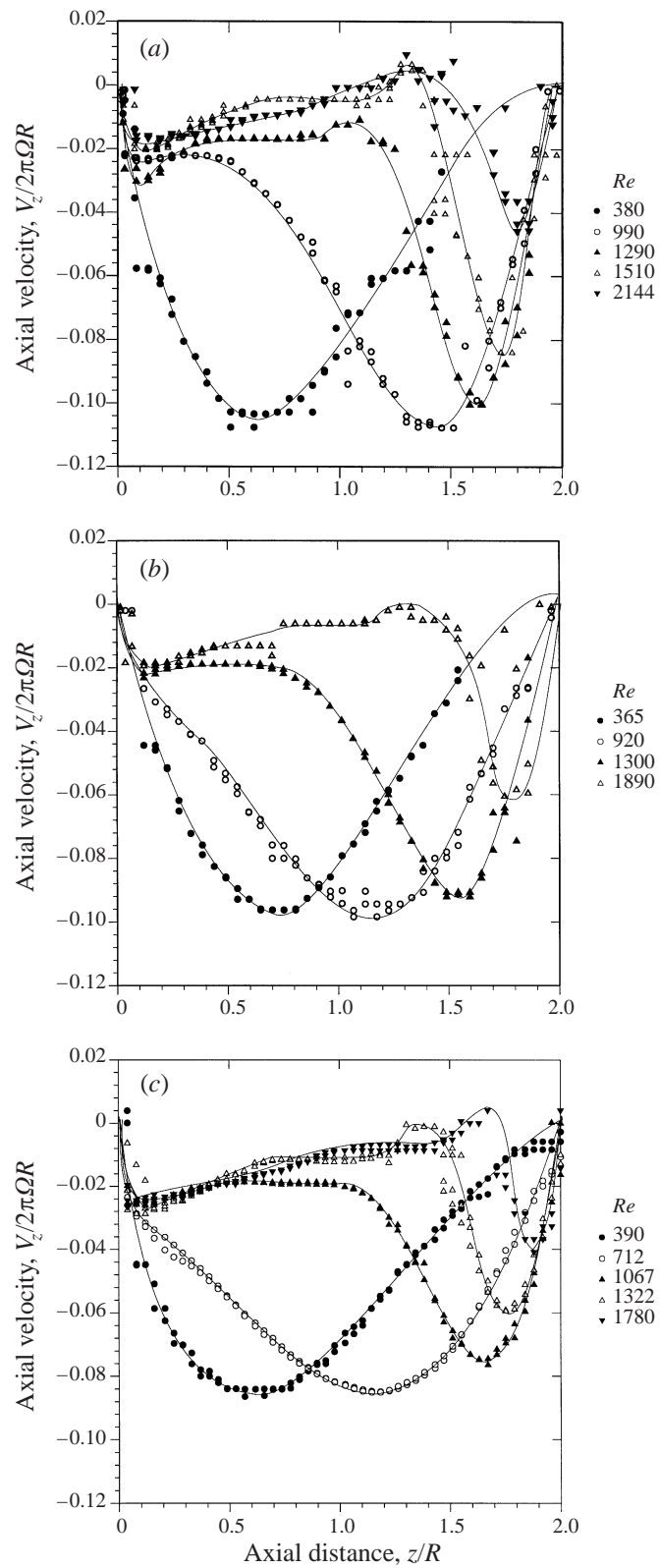


FIGURE 22 (a-c). For caption see facing page.

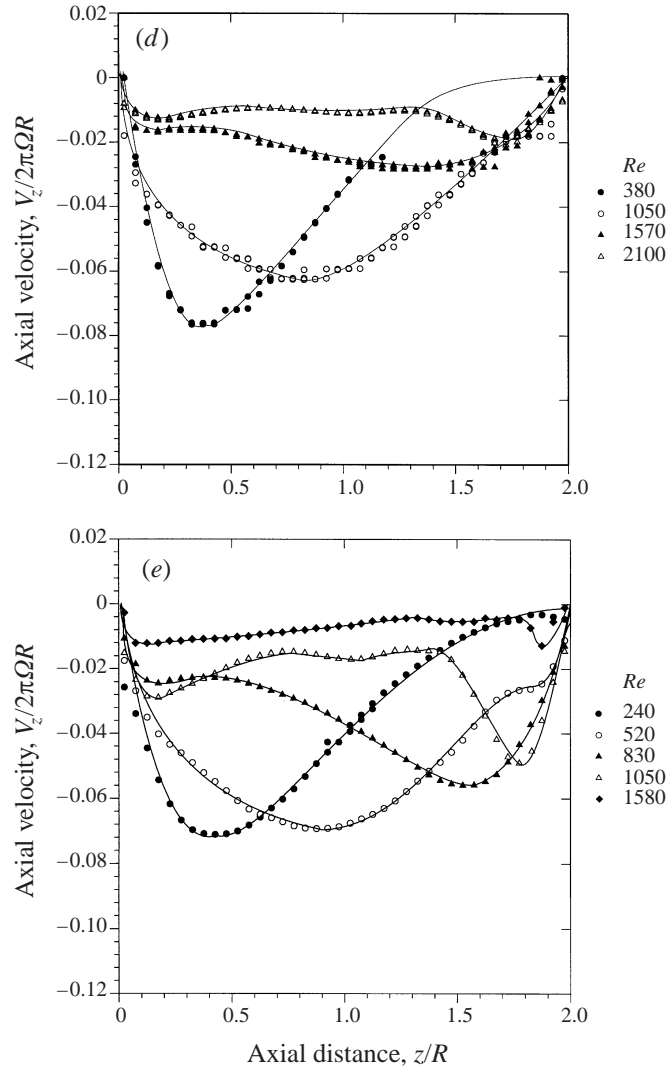


FIGURE 22. Dimensionless axial velocity measurements along centreline ( $r \approx 0$ ) for (a) Newtonian solvent (76% glycerol), (b) 45 p.p.m. polyacrylamide Boger fluid where  $El = 49 \times 10^{-6}$ , (c) 45 p.p.m. xanthan gum Boger fluid where  $El = 3.33 \times 10^{-3}$ , (d) 75 p.p.m. polyacrylamide Boger fluid where  $El = 332 \times 10^{-6}$ , (e) 75 p.p.m. xanthan gum Boger fluid where  $El = 9.4 \times 10^{-3}$ .  $H/R = 2.0$ .

close to the stationary lid as the Reynolds number is raised to  $Re = 1290$ . This peak corresponds to the stage just prior to breakdown. The velocity near the rotating lid is small in magnitude with a flat distribution governing a majority of the axial length ( $z/R < 1.1$ ). This low velocity or almost stagnant region continues to migrate to a higher axial length until a stagnation point arises and a small region of flow reversal occurs which indicates the occurrence of vortex breakdown. This vortex breakdown is shown for  $Re = 1510$  where a positive velocity is indicated at  $z/R = 1.3$ . Above  $z/R = 1.3$ , the axial velocity peak has become narrower and the magnitude of the minimum axial velocity has decreased slightly from its value prior to breakdown. Two breakdown bubbles are observed at higher Reynolds numbers such as in the case of

$Re = 2144$  and the magnitude of the minimum axial velocity is less than about half of that prior to breakdown.

The progression of the axial velocity distribution for 45 p.p.m. polyacrylamide and 45 p.p.m. xanthan gum Boger fluids are very similar to those of the Newtonian solvent with the measurements shown in figures 22(b) and 22(c), respectively. As previously mentioned, vortex breakdown occurs at larger Reynolds numbers for the 45 p.p.m. polyacrylamide Boger fluids than for the Newtonian solvent and this is reflected in the velocity profiles. At the same Reynolds number, the velocity profile for the polyacrylamide solution is less developed than that for the Newtonian fluid such that to obtain a similar velocity distribution, a higher Reynolds number is required for the polyacrylamide Boger fluid. A similar Reynolds number is required for vortex breakdown of the xanthan gum solution compared with the Newtonian solvent which is also reflected by similar velocity profiles at similar Reynolds numbers in the two cases. However, the most significant difference in the axial velocity profiles is that the minimum velocity for both the 45 p.p.m. polymer Boger fluids is lower in magnitude than for the Newtonian solvent. Prior to breakdown, the minimum velocity for the Newtonian fluids is approximately a constant of value of  $V_z/(2\pi R\Omega) \approx -0.11$  for  $380 < Re < 1290$  and seemingly independent of aspect ratio for  $1.5 < H/R < 2.5$ . However, in comparison to the Newtonian fluid, the minimum velocities were 13% and 27% lower with values of  $V_z/(2\pi R\Omega) \approx -0.096$  and  $V_z/(2\pi R\Omega) \approx -0.08$  for the 45 p.p.m. polyacrylamide and 45 p.p.m. xanthan gum Boger fluids, respectively, prior to breakdown. This decrease in magnitude of the minimum velocity correlates with the 20% and 40% increase in the minimum aspect ratio required for vortex breakdown to occur for the 45 p.p.m. polyacrylamide and 75 p.p.m. xanthan gum Boger fluids, respectively. As displayed in the existence domain plots in figures 19 and 20, the minimum aspect ratios for the Newtonian, 45 p.p.m. polyacrylamide and 45 p.p.m. xanthan gum Boger fluids was about 1.25, 1.5 and 1.75, respectively. Therefore, the results indicate that there is a strong connection between the magnitude of the minimum velocity and the minimum aspect ratio required for breakdown to occur.

Vortex breakdown does not occur for the 75 p.p.m. polyacrylamide or 75 p.p.m. xanthan gum Boger fluids for aspect ratios equal to or less than  $H/R = 2.8$ . The velocity distributions for these two Boger fluids are shown in figures 22(d) and 22(e), respectively. While showing a similar progression to the velocity profiles for the Newtonian solvent, the Boger fluids in this case do not reach very low minimum axial velocities and the velocity distributions are flatter when compared to the previous cases. There is no longer a sharp peak in the axial velocity at Reynolds numbers where vortex breakdown would occur for the Newtonian fluid. At Reynolds numbers of  $Re \approx 1500-1600$ , the velocity distribution for the Newtonian fluid (figure 22a) passes through a sharp minimum at  $z/R \approx 1.7$  to  $V_z/(2\pi R\Omega) \approx -0.084$  before increasing to a positive value in the location of the breakdown bubble at  $z/R \approx 1.3$ . However, the velocity distributions for the polyacrylamide (figure 22d) and xanthan (figure 22e) Boger fluids do not have a sharp minimum peak and the minimum velocities are 67% and 86% lower in magnitude than for the Newtonian case. For  $Re \approx 1500-1600$ , the minimum axial velocity for the polyacrylamide Boger fluid was only  $V_z/(2\pi R\Omega) \approx -0.028$  at an aspect ratio of  $z/R \approx 1.3$ , while the minimum velocity for the xanthan gum Boger fluid is only  $V_z/(2\pi R\Omega) \approx -0.012$  at an aspect ratio of  $z/R \approx 1.975$ . Therefore, the results suggest that the total suppression of breakdown for these two Boger fluids is due to the reduced magnitude of the peak axial velocity which has been caused by the action of elasticity.

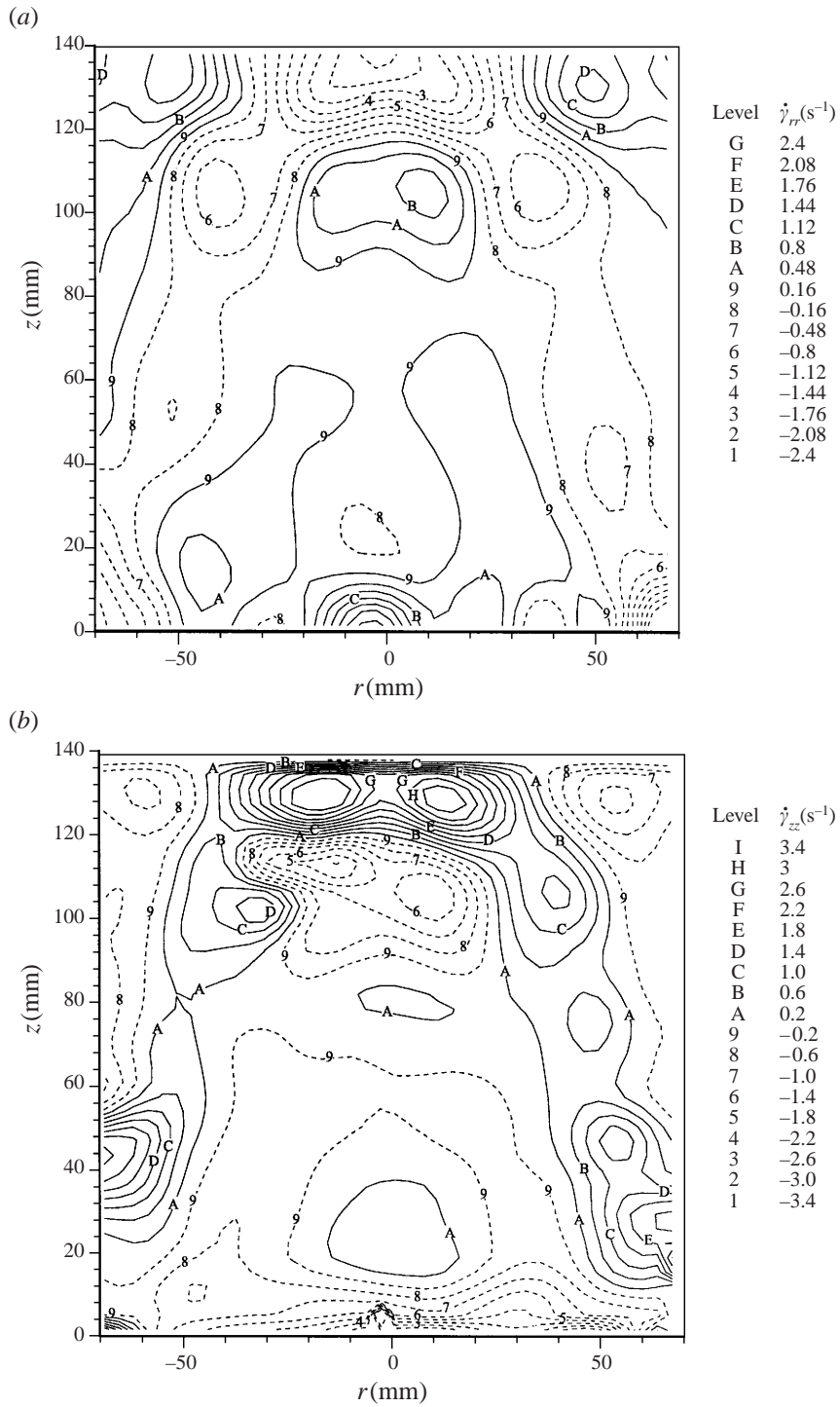


FIGURE 23. Flow field for 75 p.p.m. polyacrylamide Boger fluid at  $Re = 2100$ ,  $We = 0.7$ , and  $H/R = 2$  showing the following components of the rate-of-strain tensor (a)  $\dot{\gamma}_{rr}$  and (b)  $\dot{\gamma}_{zz}$ . Refer to figures 10 and 26 for corresponding vector field and velocity distributions, respectively.

## 6. Discussion

The confined swirling flow has been dramatically affected owing to the addition of dilute and semi-dilute concentrations of high molecular weight polymers of both flexible and semi-rigid conformation, respectively, to a Newtonian solvent. The critical aspect ratio for the occurrence of vortex breakdown is shifted to greater values as the concentration of the polymer was increased. Vortex breakdown is not observed using 75 p.p.m. of polyacrylamide or 75 p.p.m. xanthan gum for the aspect ratios examined ( $H/R < 2.8$ ). Velocity measurements have indicated that the shift in the critical aspect ratio and ultimate suppression of breakdown has arisen because of the lowering of the maximum magnitude of the dimensionless axial velocity along the centreline ( $r \approx 0$ ). The mechanisms by which elasticity has affected the axial velocity and the suppression of vortex breakdown is now discussed in more detail.

Normal stresses induced in flow arise as a result of fluid elasticity. In swirling flow, normal stresses cause a tension along curvilinear streamlines with a resultant force acting inwards, against the outward normal of these curved streamlines and in the opposite direction to inertial forces. Although the primary normal stress difference is not measurable for the low-viscosity Boger fluids, it may be estimated from the storage modulus using the relation:

$$\text{Lim}_{\gamma \rightarrow 0} N_I / 2\dot{\gamma}^2 \equiv \text{Lim}_{\omega \rightarrow 0} G' / \omega^2$$

(see Bird *et al.* 1987a). Therefore, the radial velocity in the governing boundary layer positioned on the rotating disk, which drives the whole secondary flow, is reduced by the action of normal stresses. A slight reduction in the radial velocity out of the governing boundary layer will result in a lower axial velocity down the centreline out of the boundary layer located on the stationary top lid. The waviness observed in the sectional streamlines prior to breakdown (figure 2b) results from inertial fluctuations referred to as inertial waves. These inertial waves are considered critical for the occurrence of breakdown, and their degree of waviness is controlled by the upstream axial velocity. A decrease in the axial velocity magnitude from the stationary lid therefore leads to a reduction and suppression of the degree of the waviness in the sectional streamlines and subsequently hinders the occurrence of vortex breakdown.

Extensional effects often play a role in phenomena associated with viscoelastic fluids, such as in drag reduction where extensional viscosity is associated as the cause in the reduction of turbulence through the suppression of eddy formation. It is, therefore, expected that extensional viscosity will play a role in the suppression of vortex breakdown. The apparent Trouton ratio for the Boger fluids was significantly greater than the Newtonian Trouton ratio of  $Tr = 3$ , as shown in §4.3. The polyacrylamide Boger fluids are strain rate thickening while the extensional viscosity of the xanthan gum Boger fluids is constant with strain rate. Therefore, at even small extension rates, the resistance to extension from the xanthan gum Boger fluids is higher than for Newtonian fluids and this will have an effect on the flow kinematics. For the polyacrylamide Boger fluid, reasonable extension rates are required for the extensional viscosity to be above the Newtonian value owing to its strain rate thickening behaviour. Figure 23 shows two components of the rate-of-strain tensor in the secondary flow plane, namely  $\dot{\gamma}_{rr}$  and  $\dot{\gamma}_{zz}$ , for the 75 p.p.m. polyacrylamide Boger fluid at  $Re = 2100$ . Dashed lines represent areas of negative strain rate (compressive) and solid lines represent areas of positive strain rate (extension). The areas of highest extension are situated just below the stationary lid with  $\dot{\gamma}_{zz} \approx 3.4 \text{ s}^{-1}$  and along the stationary walls from the

corner of the rotating disk where  $z < 50$  mm with  $\dot{\gamma}_{zz} \approx 2.2 \text{ s}^{-1}$ . These areas will show the highest resistance to extension in the secondary flow field for the polyacrylamide Boger fluids. The greater resistance to extension for the Boger fluids when compared to Newtonian fluids will result in a lowering of the velocity in areas of high extension rate. In particular, the minimum velocity along the centreline would be suppressed, as observed in the velocity profiles for 75 p.p.m. polyacrylamide and 75 p.p.m. xanthan gum Boger fluids in figures 22(d) and 22(e).

It is clear that even a small degree of elasticity can change the character of a swirling flow field dramatically, even when it is dominated by inertial forces. Predictions of the flow of non-Newtonian fluids are limited, including when inertia is negligible or when inertial effects are high, such as in turbulent or swirling flows. The experiments in this paper were carried out to provide experimental observations and quantitative data in a well-defined flow field, using well-characterized fluids, in order to examine the effect of elasticity on an established steady flow phenomenon observed for Newtonian fluids. As reviewed previously, inertia is the dominant force governing the flow, and, hence, the confined swirling flow experiment has demonstrated a suitable test case for validation of non-Newtonian constitutive models. This validation process is a prelude to predicting other inertia-dominated flows such as those encountered in mixing processes and drag reduction. Part 2 will examine the secondary flow field, as inertia is gradually removed from the problem and the flow becomes heavily dominated by elastic forces.

## 7. Conclusion

The secondary flow of low-viscosity dilute polyacrylamide and xanthan gum solutions has been significantly altered when compared to a Newtonian solution of similar constant viscosity. When compared to observations in the confined swirling flow of Newtonian fluids, the critical aspect ratio for the occurrence of vortex breakdown has been shifted to greater values with increasing polymer concentration such that breakdown was not observed at all for concentrations of 75 p.p.m. polyacrylamide or 75 p.p.m. xanthan gum at aspect ratios under  $H/R = 2.8$ . The existence of breakdown for any particular aspect ratio is critically dependent on the axial velocity distribution and the peak velocity near the axis of symmetry. The existence domain for breakdown has also shifted to greater values of critical Reynolds number when using 25 and 45 p.p.m. polyacrylamide, while the domain for xanthan was considerably more narrow than for a Newtonian fluid. The results indicate the effect of even a small amount of elasticity in inertia-dominated swirling flows. The provision of radial and axial velocity measurements in the secondary flow field, combined with the analysis of the alteration of the existence domain for vortex breakdown due to fluid elasticity, yields a comprehensive database for comparison with numerical solutions of the flow field.

The authors would like to thank Brook Dunstan from CSIRO for his assistance in obtaining good quality photographs, Dr D. Dunstan and Dr G. Allen at the University of Melbourne for measuring the hydrodynamic size and molecular weight of the polymers used in this work, respectively, and Dr K. C. Tam from Nanyang University for measuring the rheological properties of the polymer solutions using the Contraves LS40 rheometer. The work on viscoelastic fluid mechanics at the University of Melbourne is funded by a Special Investigators Grant for the Australian Research Council awarded to D.V.B.

## REFERENCES

- ADRIAN, R. J. 1991 Particle-imaging techniques for experimental fluid mechanics. *Ann. Rev. Fluid Mech.* **23**, 261–304.
- BATCHELOR, G. K. 1970 The stress system in a suspension of force-free particles. *J. Fluid Mech.* **41**, 545–570.
- BATCHELOR, G. K. 1971 The stress generated in a non-dilute suspension of elongated particles by pure shearing motion. *J. Fluid Mech.* **46**, 813–829.
- BENJAMIN, T. B. 1962 Theory of the vortex breakdown phenomenon. *J. Fluid Mech.* **14**, 593–629.
- BERGER, S. A. & ERLEBACHER, G. 1995 Vortex breakdown incipience: theoretical considerations. *Phys. Fluids* **7**, 972–982.
- BIEN, F. & PENNER, S. S. 1970 Velocity profiles in steady and unsteady rotating flows for a finite cylindrical geometry. *Phys. Fluids* **13**, 1665–1671.
- BINNINGTON, R. J., TROUP, G. J. & BOGER, D. V. 1983 A low cost laser-speckle photographic technique for velocity measurement in show flows. *J. Non-Newtonian Fluid Mech.* **12**, 255–267.
- BIRD, R. B., ARMSTRONG, R. C. & HASSANGER, O. 1987a *Dynamics of Polymeric Liquids. Volume 1: Fluid Mechanics*, 2nd edn. Wiley Interscience.
- BIRD, R. B., CURTISS, C. F., ARMSTRONG, R. C. & HASSANGER, O. 1987b *Dynamics of Polymeric Liquids. Volume 2: Kinetic Theory*, 2nd edn. Wiley Interscience.
- BOGER, D. V. 1977/78 A highly elastic constant viscosity fluid. *J. Non-Newtonian Fluid Mech.* **3**, 87–91.
- BÖHME, G., RUBART, L. & STENGER, M. 1992 Vortex breakdown in shear-thinning liquids: experiment and numerical simulation. *J. Non-Newtonian Fluid Mech.* **45**, 1–20.
- BÖHME, G., VOSS, R. & WARNECKE, W. 1985 Die frei oberfläche einer flüssigkeit über einer rotierenden scheibe. *Rheol. Acta* **24**, 22–23.
- BROERSMA, S. 1960 Rotational diffusion constant of a cylindrical particle. *J. Chem. Phys.* **32**, 1626–1631.
- BROWN, G. L. & LOPEZ, J. M. 1990 Axisymmetric vortex breakdown. Part 2. Physical mechanisms. *J. Fluid Mech.* **221**, 553–576.
- BRYDON, A. & THOMPSON, M. 1998 A trapped wave model for confined vortex breakdown. In *Proc. 13th Australasian Fluid Mech. Conf.* In press.
- BUCHAVE, P., JAKOBSEN, M. L., WESTERGAARD, C. H. & SØRENSEN, J. N. 1991 PIV: measurement of the early transition of a rotating flow in a closed cylinder. In *Proc. 4th Intl Conf. Laser Anemometry, Advances and Applications*, Cleveland, USA.
- CARREAU, P. J. 1968 Rheological equations from molecular network theories. PhD dissertation, University of Wisconsin.
- CHIAO, S.-M. F. & CHANG, H.-C. 1990 Instability of a Criminale–Ericksen–Filbey fluid in a disk-and-cylinder system. *J. Non-Newtonian Fluid Mech.* **36**, 361–394.
- DAY, C., HARRIS, J. A., SORIA, J., BOGER, D. V. & WELSH, M. C. 1996 Behaviour of an elastic fluid in cylindrical swirling flow. *Exp. Therm. Fluid Sci.* **12**, 250–255.
- DEBBAUT, B. & HOCQ, B. 1992 On the numerical simulation of axisymmetric swirling flows of differential viscoelastic liquids: the rod climbing effect and the Quelleffekt. *J. Non-Newtonian Fluid Mech.* **43**, 103–126.
- DELERY, J. M. 1994 Aspects of vortex breakdown. *Prog. Aero. Sci.* **30**, 1–59.
- DOI, M. & EDWARDS, S. F. 1986 *The Theory of Polymer Dynamics*, Clarendon, Oxford.
- DONTULA, P., PASQUALI, M., SCRIVEN, L. E. & MACOSKO, C. W. 1998 Can extensional viscosity be measured with opposed nozzle devices? *Rheol. Acta*. Submitted.
- DURST, F., LEHMANN, B. & TROPEA, C. 1981 Laser-dropller system for rapid scanning of flow fields. *Rev. Sci. Instrum.* **52**, 1676–1681.
- EISENBRAND, G. D. & GODDARD, J. D. 1982 Birefringence and pressure drop for the orifice flow of a polymer solution. *J. Non-Newtonian Fluid Mech.* **11**, 37–52.
- ELLE, B. J. 1960 On the breakdown at high incidences of the leading edge vortices on delta wings. *J. R. Aero. Soc.* **64**, 596.
- ESCUDIER, M. P. 1984 Observations of the flow produced in a cylindrical container by a rotating endwall. *Exps Fluids* **2**, 189–196.
- ESCUDIER, M. P. 1988 Vortex breakdown: Observations and Explanations. *Prog. Aero. Sci.* **25**, 189–229.

- ESCUDIER, M. P. & CULLEN, L. M. 1996 Flow of a shear-thinning liquid in a cylindrical container with a rotating end wall. *Expl Therm. Fluid Sci.* **12**, 381–387.
- FERRY, J. D. 1980 *Viscoelastic Properties of Polymers*, 3rd edn. John Wiley.
- FLORY, P. J. 1953 *Principles in Polymer Chemistry*. Cornell University Press, New York.
- FUJIMURA, K., KOYAMA, H. S. & HYUN, J. M. 1997 Time-dependent vortex breakdown in a cylinder with a rotating lid. *Trans. ASME I: J. Fluids Engng* **119**, 450–453.
- FULLER, G. G., CATHEY, C. A., HUBBARD, B. & ZEBROWSKI, B. E. 1987 Extensional viscosity measurements of low-viscosity fluids. *J. Rheol.* **31**, 235–249.
- GELFGAT, A. YU., BAR-YOSEPH, P. Z. & SOLAN, A. 1996 Stability of confined swirling flow with and without vortex breakdown. *J. Fluid Mech.* **311**, 1–36.
- GRAY, C., GREATED, C. A., MCCLUSKEY, D. R. & EASSON, W. J. 1991. Analysis of the scanning beam PIV illumination system. *Meas. Sci. Technol* **2**, 717–724.
- HALL, M. G. 1972 Vortex Breakdown. *Ann. Rev. Fluid Mech.* **4**, 195–218.
- HARVEY, J. K. 1962 Some observations of the vortex breakdown phenomena. *J. Fluid Mech* **14**, 585–592.
- HERMANSKY, C. G. & BOGER, D. V. 1995 Opposing jet viscometry of fluids with viscosity approaching that of water. *J. Non-Newtonian Fluid Mech.* **56**, 1–14.
- HILL, C. T. 1969 Viscoelastic fluid flow in the disk and cylinder system. PhD dissertation, University of Wisconsin.
- HILL, C. T. 1972 Nearly visometric flow of viscoelastic fluids in the disk and cylinder system. II: Experimental. *Trans. Soc. Rheol.* **16**, 213–245.
- HILL, C. T., HUPPLER, J. D. & BIRD, R. B. 1966 Secondary flows in the disk-and-cylinder system. *Chem. Engng Sci.* **21**, 815–817.
- HOLDZWARTH, G. 1978 Molecular weight of xanthan polysaccharide. *Carbohydr. Res.* **66**, 173–186.
- HOURIGAN, K., GRAHAM, L. J. W. & THOMPSON, M. C. 1995 Spiral streaklines in pre-vortex breakdown regions of axisymmetric swirling flows. *Phys. Fluids* **7**, 3126–3128.
- JONES, J. P. 1960 The breakdown of vortices in separated flow. Dept Aero. Astro., University of Southampton, *Rep. no.* 140.
- KEANE R. D. & ADRIAN, R. J. 1991 Optimization of particle image velocimeters. Part II. Multiple pulsed systems. *Meas. Sci. Technol* **2**, 963–974.
- KELLER, J. J. 1995 On the interpretation of vortex breakdown. *Phys. Fluids* **7**, 1965–1702.
- KRAMER, J. M. 1969 Analytical study of viscoelastic fluid flow in the disc and cylinder system. PhD dissertation, University of Wisconsin.
- KRAMER, J. M. & JOHNSON, M. W. 1972 Nearly visometric flow in the disk and cylinder system. I: Theoretical. *Trans. Soc. Rheol.* **16**, 197–212.
- LAMBOURNE, N. C. & BRYER, D. W. 1961 The bursting of leading-edge vortices—some observations and discussion of the phenomenon. *Aero. Res. Council. Reports & Memoranda, R & M no.* 3282, 1–36.
- LANDRETH, C. C. & ADRIAN, R. J. 1988 Measurement and refinement of velocity data using high image density analysis in particle image velocimetry. In *Proc. 4th Intl Symp. Applications of Laser Anemometry to Fluid Mech.* (ed. R. J. Adrian, A. Asanuma, D. Durao, F. Durst, W. Whitelaw) pp. 491–497, Lisbon.
- LAWLAR, J. V., MULLER, S. J., BROWN, R. A. & ARMSTRONG, R. C. 1986 Laser Doppler velocity measurements of velocity field and transitions in viscoelastic fluids. *J. Non-Newtonian Fluid Mech.* **20**, 51–92.
- LAWSON, N. J., COUPLAND, J. M. & HALLIWELL, N. A. 1997 A generalised optimisation method for double pulsed particle image velocimetry. *Optics Lasers Engng* **27**, 637–656.
- LEE, M. Y. & SEXTON, S. 1994 The limitations of the Carri-Med controlled stress rheometer. Department of Chemical Engineering, University of Melbourne.
- LEIBOVICH, S. 1978 The structure of vortex breakdown. *Ann. Rev. Fluid Mech.* **10**, 221–246.
- LEIBOVICH, S. 1984 Vortex stability and breakdown: Survey and extension. *Amer. Inst. Aero. Astro. J.* **22**, 1192–1206.
- LIAO, C. B. & YOUNG, D. L. 1995 Numerical simulation of three-dimensional vortex flow within a cylindrical tank with a rotating end-wall. In *Numerical Methods in Laminar and Turbulent Flow '95* (ed. C. Taylor & P. Durbetaki) vol. 9, pp. 155–166.
- LOPEZ, J. M. 1990 Axisymmetric vortex breakdown. Part 1. Confined swirling flow. *J. Fluid Mech.* **221**, 533–552.

- LOPEZ, J. M. 1994 On the bifurcation structure of axisymmetric vortex breakdown in a constricted pipe. *Phys. Fluids* **6**, 3683–3693.
- LOPEZ, J. M. 1995 Unsteady swirling flow in an enclosed cylinder with reflectional symmetry. *Phys. Fluids* **7**, 2700–2714.
- LOPEZ, J. M. & PERRY, A. D. 1992 Axisymmetric vortex breakdown. Part 3. Onset of periodic flow and chaotic advection. *J. Fluid Mech.* **234**, 449–471.
- LUDWEIG, H. 1961 Contribution to the explanation of the instability of vortex cores above lifting delta wings. *Aero. Versuchsanstalt, Gottingen, Rep.* AVA/61 A01.
- LUGT, H. J. & ABBOUD, M. 1987 Axisymmetric vortex breakdown with and without temperature effects in a container with a rotating lid. *J. Fluid Mech.* **179**, 179–200.
- MEINHART, C. D., PRASAD, A. K. & ADRIAN, R. J. 1993 Parallel digital processor system for particle image velocimetry. *Meas. Sci. Technol.* **4**, 619–626.
- NIRSCHL, J. P. & STEWART, W. E. 1984 Computation of viscoelastic flow in a cylindrical tank with a rotating lid. *J. Non-Newtonian Fluid Mech.* **16**, 233–250.
- NORTON, L. T., GOODALL, D. M., FRANGOU, S. A., MORRIS, E. R. & REES, D. A. 1984 Mechanism and dynamics of conformational ordering in xanthan polysaccharide. *J. Mol. Biol.* **175**, 371–394.
- PARADOSSI, G. & BRANT, D. A. 1982 Light scattering study of a series of xanthan fractions in aqueous solution. *Macromolecules* **15**, 874–879.
- PECKHAM, D. H. & ATKINSON, S. A. 1957 Preliminary results of low speed wind tunnel tests on a gothic wing of aspect ratio 1.0. *Aeronautical Research Council CP* **508**.
- PERRY, A. E. & STEINER, T. R. 1987 Large-scale vortex structures in turbulent wakes behind bluff bodies. Part 1. Vortex formation processes. *J. Fluid Mech.* **174**, 233–270.
- PICKERING, J. D. & HALLIWELL, N. A. 1985 Particle image velocimetry: a new field measurement technique. In *Optical Measurement in Fluid Mechanics, Inst. Phys. Conf. Series no. 77* (ed. A. Hilger), Bristol.
- PRASAD, A. K. & ADRIAN, R. J. 1993 Stereoscopic particle image velocimetry applied to liquid flows. *Exps Fluids* **15**, 49–60.
- PRASAD, A. K., ADRIAN, R. J., LANDRETH, C. C. & OFFUTT, P. W. 1992 Effect of resolution on the speed and accuracy of particle image velocimetry interrogation. *Exps Fluids* **13**, 105–116.
- ROESNER, K. G. 1990 Recirculation zones in a cylinder with rotating lid. In *Topological Fluid Mechanics* (ed. H. K. Moffatt & A. Tsinober), pp. 699–708, Cambridge University Press.
- RONNENBERG, B. 1977 Ein selbstjustierendes 3-omponenten-Laserdoppleranemometer nach dem Vergleichsstrahlverfahren, angewandt für Untersuchungen in einer stationären zylindersymmetrischen Drehströmung mit einem Rückstromgebiet. *Max-Planck-Inst. Bericht* **20**.
- RUSAK, Z. 1996 Axisymmetric swirling flow around a vortex breakdown point. *J. Fluid Mech.* **323**, 79–105.
- SARPAKAYA, T. 1971 On stationary and travelling vortex breakdowns. *J. Fluid Mech.* **45**, 545–559.
- SATO, T., NORISUYE, T. & FUJITA, H. 1984 Double-stranded helix of xanthan in dilute solution: further evidence. *Polym. J.* **16**, 341–350.
- SCHUNK, P. R., DESANTOS, J. M. & SCRIVEN, L. E. 1990 Flow of Newtonian liquids in opposed-nozzles configuration. *J. Rheol.* **34**, 387–414.
- SIGINER, A. 1991 Viscoelastic swirling flow with free surface in cylindrical chambers. *Rheol. Acta* **30**, 159–174.
- SØRENSEN, J. N. & CHRISTENSEN, E. A. 1995 Direct numerical simulation of rotating fluid flow in a closed cylinder. *Phys. Fluids* **7**, 764–778.
- SØRENSEN, J. N. & DAUBE, O. 1989 Direct simulation of flow structures initiated by a rotating cover in a cylindrical vessel. In *Advances in Turbulence 2* (ed. H. H. Fernholz & H. E. Fiedler), pp. 383–390, Springer.
- SPALL, R. E. 1996 Transition from spiral- to bubble-type vortex breakdown. *Phys. Fluids* **8**, 1330–1332.
- SPOHN, A., MORY, M. & HOPFINGER, E. J. 1993 Observation of vortex breakdown in an open cylindrical container with a rotating bottom. *Exps Fluids* **14**, 70–77.
- SPOHN, A., MORY, M. & HOPFINGER, E. J. 1998 Experiments on vortex breakdown in a confined flow generated by a rotating disc. *J. Fluid Mech.* **370**, 73–99.
- SPRIGGS, T. W., HUPPLER, J. D. & BIRD, R. B. 1966 *Trans. Soc. Rheol.* **10**, 191.
- SQUIRE, H. B. 1960 Analysis of the vortex breakdown phenomenon. *Miszallaneen der Angewandten Mechanik*, Berlin, Akademie, 306–312.

- STOKES, J. R. 1998 Swirling flow of viscoelastic fluids. PhD dissertation, University of Melbourne.
- STOKES, J. R., GRAHAM, L. J. W., LAWSON, N. J. & BOGER, D. V. 2001 Swirling flow of viscoelastic fluids. Part 2. Elastic effects. *J. Fluid Mech.* **429**, 117–153.
- TAM, K. C. & TIU, C. 1989*a* A low-viscosity, highly elastic ideal fluid. *J. Non-Newtonian Fluid Mech.* **31**, 163–177.
- TAM, K. C. & TIU, C. 1989*b* Steady and dynamic properties of aqueous polymer solutions. *J. Rheol.* **33**, 257–280.
- TANNER, R. I. 1985 Constitutive equations for the computing person. In *Viscoelasticity and Rheology* (ed. A. S. Lodge, M. Renardy & J. A. Nohel), pp. 421–439. Academic Press.
- TSITVERBILT, N. 1993 Vortex breakdown in a cylindrical container in the light of continuation of a steady solution. *Fluid Dyn. Res.* **11**, 19–35.
- UNG, T., GIERSIG, M., DUNSTAN, D. & MULVANEY, P. 1997 Spectroelectrochemistry of colloidal silver. *Langmuir* **13**, 6393–6399.
- VALENTINE, D. T. & JAHNKE, C. C. 1994 Flows induced in a cylinder with both end walls rotating. *Phys. Fluids* **6**, 2702–2710.
- VOGEL, H. U. 1968 Experimentelle Ergebnisse über die laminare Strömung in einen zylindrischen Gehäuse mit darin rotierender Scheibe. *Max-Planck-Inst. Bericht* **6**.
- VOGEL, H. U. 1975 Rückströmungsblasen in Drallströmungen. In *Festschrift zum 50-jährigen Bestehen des MPI für Strömungsforschung*, pp. 263–272. Hubert, Göttingen.
- WANG, S. & RUSAK, Z. 1997 The dynamics of a swirling flow in a pipe and transition to axisymmetric vortex breakdown. *J. Fluid Mech.* **340**, 177–223.
- WATSON, J. P. & NEITZEL, G. P. 1996 Numerical evaluation of a vortex-breakdown criterion. *Phys. Fluids* **8**, 3063–3071.
- WERLÉ, H. 1960 Sur l'éclatement des tourbillons d'apex d'une aile delta aux faibles vitesses. *La Recherche Aérospatiale*, **74**, 23–30.
- WÜSCH, O. & BÖHME, G. 1996 On torsionally driven viscoelastic flow in a cylindrical vessel. In *Proc. XIIIth Intl Congr. Rheology* (ed. A. Ait-Kadi, J. M. Dealy, D. F. James & M. C. Williams), pp. 846–848, Laval University.
- YOUNG, C. Y., MISSEL, P. J., MAZER, N. A. & BENEDEK, G. B. 1978 Deduction of micellar shape from angular dissymmetry measurements of light scattered from aqueous sodium dodecyl sulfate solutions at high sodium chloride concentrations. *J. Phys. Chem.* **82**, 1375–1378.
- ZIRNSAK, M. 1995 Rheology and axisymmetric entry flow of dilute and semi-dilute solutions of semi-rigid molecules. PhD dissertation, University of Melbourne.